Journal of Alloys and Compounds 906 (2022) 164384

Contents lists available at ScienceDirect

Journal of Alloys and Compounds

journal homepage: www.elsevier.com/locate/jalcom

Structure and properties of phases in the $Cu_{2-X}Se$-Sb_2Se_3 system. The $Cu_{2-X}Se$-Sb_2Se_3 phase diagram

M.A. Shtykova[a,*], M.S. Molokeev[b,c], B.A. Zakharov[d,e], N.V. Selezneva[f], A.S. Aleksandrovsky[b,c], R.S. Bubnova[g], D.N. Kamaev[h], A.A. Gubin[i], N.N. Habibullayev[a], A.V. Matigorov[j], E.V. Boldyreva[d,e], O.V. Andreev[a,k]

[a] Department of Inorganic and Physical Chemistry, Institute of Chemistry, Tyumen State University, Volodarsky str. 6, 625003 Tyumen, Russia
[b] Kirensky Institute of Physics, Federal Research Center KSC SB RAS, Akademgorodok Str. 50, Building 38, 660036 Krasnoyarsk, Russia
[c] Siberian Federal University, Svobodnyj av. 79, 660079 Krasnoyarsk, Russia
[d] Boreskov Institute of Catalysis SB RAS, Lavrentiev Ave. 5, 630090 Novosibirsk, Russia
[e] Novosibirsk State University, Pirogova str. 2, 630090 Novosibirsk, Russia
[f] Department of Condensed Matter Physics and Nanoscale Systems, Institute of Natural Sciences and Mathematics, Ural Federal University, Mira str. 19, 620002 Yekaterinburg, Russia
[g] Grebenshchikov Institute of Silicate Chemistry, Russian Academy of Sciences, Makarov Emb., 2, 199034 St. Petersburg, Russia
[h] Department of Physical and Applied Chemistry, Institute of Natural Sciences and Mathematics, Kurgan State University, Sovetskaya str. 2, b. 4, 640020 Kurgan, Russia
[i] Laboratory of Electron and Probe Microscopy, REC "Nanotechnology", Tyumen State University, Volodarsky str. 6, 625003 Tyumen, Russia
[j] Engineering Center of Composite Materials Based on Tungsten Compounds and Rare Earth Elements, Tyumen State University, Volodarsky str. 6, 625003 Tyumen, Russia
[k] Institute of Solid State Chemistry, Ural Branch, Russian Academy of Sciences, Pervomaiskaya str. 91, 620990 Yekaterinburg, Russia

ARTICLE INFO

Article history:
Received 7 November 2021
Received in revised form 20 February 2022
Accepted 25 February 2022
Available online 28 February 2022

Keywords:
Phase equilibria
Phase diagram
High-temperature X-ray diffraction
Redlich-Kister polynomial model
Scanning electron microscopy
Differential scanning calorimetry

ABSTRACT

The phase diagram of the $Cu_{2-X}Se$-Sb_2Se_3 system is revisited to clarify ambiguity/disagreement in previously reported data. Ternary Cu_3SbSe_3 and $CuSbSe_2$ compounds were obtained. In order to confirm that the phases have been identified correctly, crystal structures were solved, and the energy band gaps measured. For the sample containing 75 mol% Sb_2Se_3 and 25 mol% $Cu_{1.995}Se$ the temperature range of the stability of the high-temperature $CuSb_3Se_5$ phase was determined for the first time. This phase is formed at 445 °C, decomposes following a peritectic reaction at 527 °C, and can be quenched. A high-temperature X-ray diffraction study of a sample containing 75 mol% Sb_2Se_3 and 25 mol% Cu_2Se allowed us to measure the thermal expansion of the $CuSbSe_2$ and Sb_2Se_3 phases present in the sample. The anisotropy of thermal expansion of $CuSbSe_2$ is similar to that of As_2S_3 (orpiment); thermal expansion of Sb_2Se_3 is similar to that of AsS (realgar). The 6 balance equations of the invariant phase transformations involving all the ternary compounds existing in the $Cu_{2-X}Se$-Sb_2Se_3 system were suggested for the first time. The temperature and the enthalpies of all these transformations were measured. A phase diagram of the $Cu_{2-X}Se$-Sb_2Se_3 system was found for the first time in all the range of concentrations at temperatures from ambient to the complete melting. This diagram takes into consideration the phase equilibria that involve all the ternary compounds that are possible in this system. The liquidus of the $Cu_{2-X}Se$-Sb_2Se_3 system was calculated according to Redlich-Kister equation; it agrees with the experimental data within 1–17 °C.

1. Introduction

Materials based on Sb_2Se_3 (*n*-type semiconductor) and $Cu_{2-X}Se$ (*p*-type semiconductor) are candidates to substitute the Bi_2Te_3 and Sb_2Te_3, respectively, in thermoelectric converters (TEGs) [1,2] and electronic devices [3,4].

The $Cu_{2-X}Se$ (x = 0–0.25) phase, as well as $Cu_{2-X}S$ [5], is a self-doped *p*-type semiconductor with a mixed ionic-electronic conductivity: $\rho = 10^{-4}$–10^{-5} Ω m, and κ = 1 W/(m K). The Seebeck coefficient for α-Cu_2Se is in the range from 60 to 100 mV/K (300–350 K), and for β-Cu_2Se (420–1000 K), from 80 to 300 mV/K (420–1000 K) [2].

* Corresponding author.
E-mail address: m.a.shtykova@utmn.ru (M.A. Shtykova).

https://doi.org/10.1016/j.jallcom.2022.164384
0925-8388/

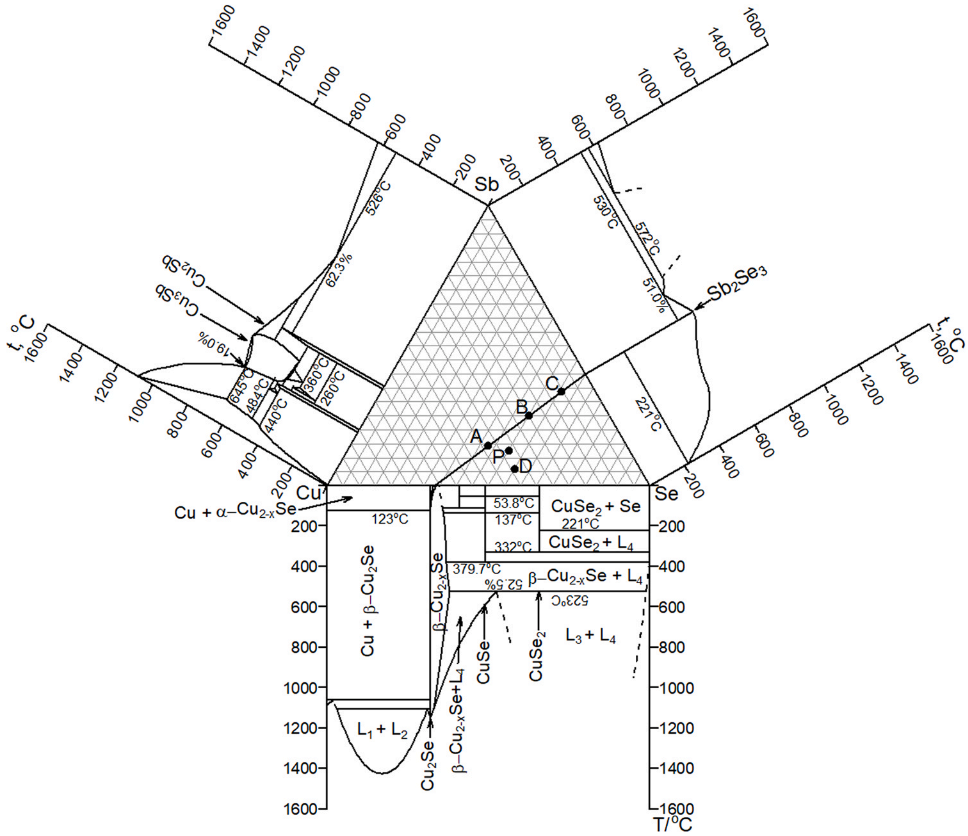

Fig. 1. The Cu-Sb-Se ternary system. Designations: A – Cu_3SbSe_3, B – $CuSbSe_2$, C – $Cu_{10.53}Sb_{33.78}Se_{55.68}$, D – $Cu_{38.8}Sb_{6.10}Se_{55.1}$, P – Cu_3SbSe_4 (permingheatite) (the phases were identified in [19]). Diagrams of binary systems Cu-Sb [20], Sb-Se [21], Cu-Se [22] are plotted on the sides of the triangle.

The Seebeck coefficient for Sb_2Se_3 at 300 K $\alpha \approx 1200$ mV/K [1] that is several times higher than the respective values for bismuth telluride or antimony telluride [6–8], as well as for their base alloys [9–11]. However, Sb_2Se_3 has low electric conductivity: $\sigma \approx 10^{-6}\ \Omega^{-1}$ cm^{-1} at 300 K [12]. It is promising to study $Cu_{2-X}Se$ and Sb_2Se_3 based solid solutions in the Cu-Sb-Se ternary system (Fig. 1), since it is known that solid solutions often have improved thermoelectric parameters as compared with pure components [13–18].

The synthesis of Cu_2Se samples involves copper precipitation, so the thus-produced selenide phase has its stoichiometry shifting to $Cu_{2-X}Se$ [22], X values being not specified in that study. The $Cu_{2-X}Se$ polymorphs differ significantly from each other in X values (Fig. 1). The low-temperature phase α-$Cu_{2-X}Se$ exists at temperatures up to 130 °C [2,23,24]; it crystallizes in the monoclinic system: a = 14,087 (Å), b = 20,481 (Å), c = 4145 (Å), β = 90,38° [25]; a = 7.1379(4) (Å), b = 12.3823(7) (Å), c = 27.3904(9) (Å), β = 94.308º [26]. At 130 °C, α-$Cu_{2-X}Se$ transforms to β-$Cu_{2-X}Se$, the cubic high-temperature phase: a = 5.859(1) Å [26]; a = 5854 Å [27], space group $Fm3m$ [26,27]. The congruent melting temperature was measured using differential thermal analysis to be 1117 °C [28], while use of drop calorimeter [29] resulted in the same melting temperature 1117 °C and specific heat 9055 J/mol. Glazov et al. reported the highest copper selenide melting temperature, equal to 1148 ± 1 °C, for a sample of $Cu_{1.994}Se$ [22]. Korzhuev et al. measured the highest melting temperature 1148 °C for $Cu_{1.99}Se$ [30]. Above the melting point, only liquid exists in the Cu-Se system (Fig. 2A). In [30], a stacked diagram of the $Cu_{2-X}Se$ solid solution area is presented, the high-temperature part of which was not studied by thermal analysis methods.

Alpha and beta phases exist as independent areas of solid solutions. The $\alpha \rightarrow \beta$ transition occurs at 140 °C and is accompanied by the formation of the β-phase and the elementary substance Cu. In the Cu-Se system, the composition of copper selenide $Cu_{2-X}Se$, which is in equilibrium with pure copper, is unknown. The dependence of this composition on the annealing temperature is also unknown.

Sb_2Se_3 crystallizes in the orthorhombic crystal system: structural type Sb_2S_3, Z = 4; previously reported data on space groups (SG) (No 62) and unit cells parameters with e.s.d.s reported in the papers [31–35], are summarized in the Table 1.

The melting temperature of Sb_2Se_3 was measured as 611 °C in the paper [36] using differential thermal analysis; its heat of congruent melting was measured as either 50.2 ± 4.2 kJ/mol in the paper [37] or 54.4 ± 4.2 kJ/mol in the paper [38] using drop calorimeter.

The $Cu_{2-X}Se$-Sb_2Se_3 system is a section of the Cu-Sb-Se triangle (Fig. 1). Karup-Moller constructed the 350, 400, 450, 500, 600, and 700 °C isothermal sections of the Cu-Sb-Se triangle when studying 264 samples by the microprobe analysis using a JEOL Superprobe 733 [19]. From the data of [19], the results from the Cu_2Se($Cu_{2-X}Se$)-Sb_2Se_3 section are selected (Fig. 2B).

Majsztrik et al. [47] succeeded to prepare a single-phase Cu_3SbSe_3 sample by melt-quenching a 3Cu:1Sb:3Se batch followed by annealing at temperatures between 325 and 400 °C during up to 120 h. Quenching of a 3Cu:1Sb:3Se melt maintained at 500 or 900 °C without subsequent annealing yielded three-phase samples containing Cu_2Se, $CuSbSe_2$, and Cu_3SbSe_3. Annealing of the as-quenched three-phase sample at a temperature between 320 °C and 400 °C yielded Cu_3SbSe_3 due to the reaction between Cu_2Se and $CuSbSe_2$ controlled by diffusion rates in the solid state. The authors of [47] have measured the microhardness of the grains of Cu_2Se, Cu_3SbSe_3 and $CuSbSe_2$ using polished samples and a nanoindenter (Hysitron, TriboIndenter) with a diamond Berkovitch tip. According to [47], the

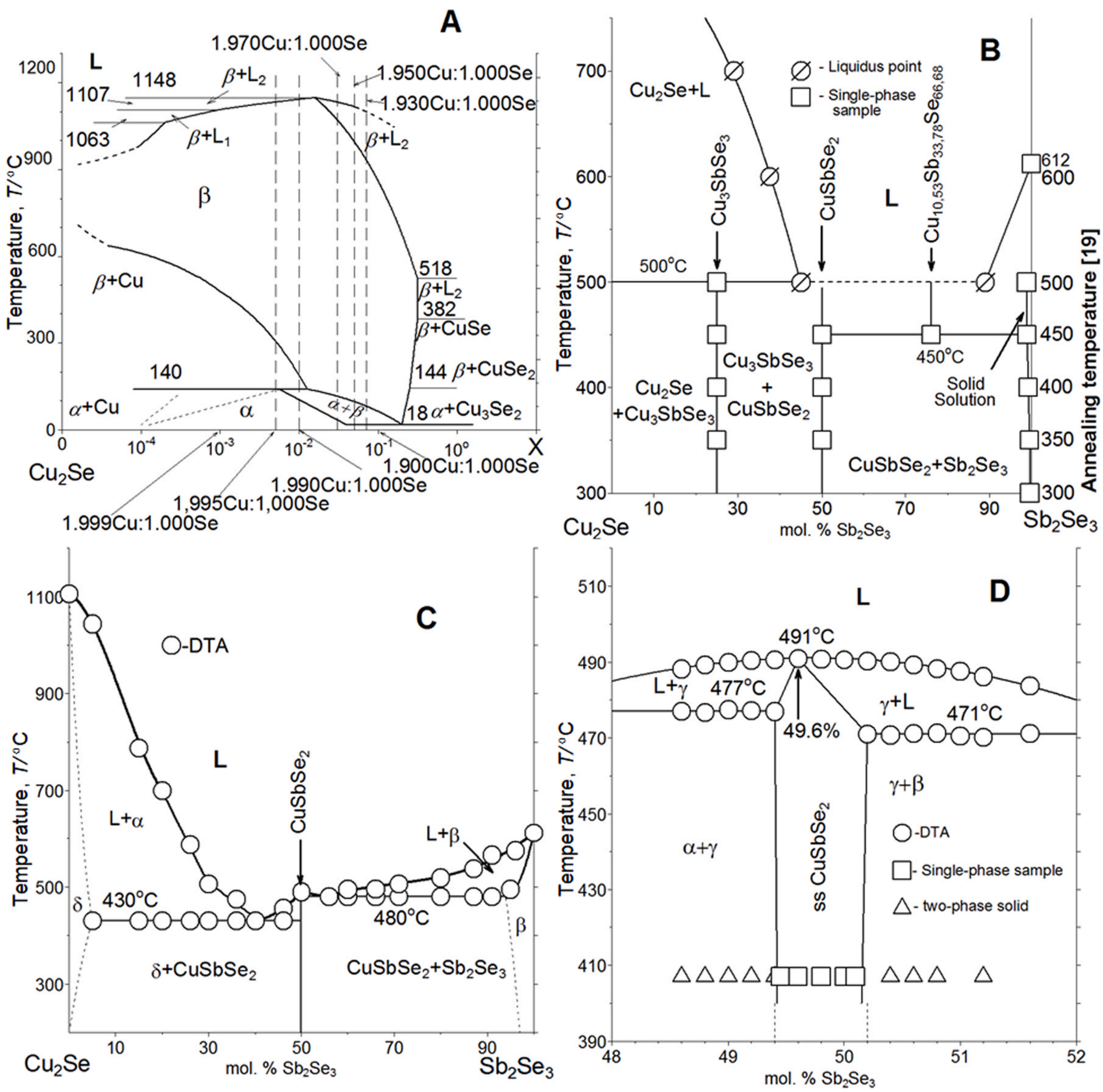

Fig. 2. Phase diagrams of systems. (A) is the area of the $Cu_{2-X}Se$ solid solution. The x axis is the nonstoichiometry of the copper content [30]. Vertical dotted lines highlight a number of compositions. (B) – phase states of the samples in the section Cu_2Se-Sb_2Se_3 according to the study of the Cu-Sb-Se system in isothermal sections [19]. (C) – phase diagram of the Cu_2Se-Sb_2Se_3 system according to [39]. (D) – area of $CuSbSe_2$ phase based solid solution [40].

Table 1
Literature data on SG (No 62) and unit cell parameters for Sb_2Se_3 (Space group is the same in all 4 papers, two different settings were used for structure refinement), Z = 4.

Ref.	Setting	Unit cell parameters			
		a, (Å)	*b*, (Å)	*c*, (Å)	*V*, (Å^3)
[31]	*Pnma*	11.794(1)	3.986(1)	11.648(1)	547.583
[32]	*Pnma*	11.7938(9)	3.9858(6)	11.6478(7)	547.54
[33]	*Pnma*	11.744(4)	3.955(2)	11.588(5)	538.23
	(Pbnm)	(11.588(5))	(11.744(4))	(3.955(2))	
[34]	*Pnma*	11.77(1)	3.962(7)	11.62(1)	541.872
	(Pbnm)	(11.62(1))	(11.77(1))	(3.962(7))	
[35]	*Pnma*	11.780	3.985	11.633	546.09
	(Pbnm)	(11.633)	(11.780)	(3.985)	

values of the microhardness of the samples Cu_3SbSe_3 and $CuSbSe_2$ with different thermal history were very close (about 35000 MPa). The microhardness of the Cu_2Se phase was smaller (8000 MPa).

Glazov et al. in the paper [39] described phase equilibria in the Cu_2Se-Sb_2Se_3 system by a phase diagram with one congruently melting compound, namely $CuSbSe_2$, which divided the diagram into two simple eutectic diagrams with limited solid solubility (Fig. 2C).

Golovei et al. in the paper [40] determined the extension of $CuSbSe_2$-based solid solution as 49.5–50.1 mol% Sb_2Se_3. The maximum melting temperature (491 ± 3 °C) corresponds to the Sb_2Se_3 content 49.6 mol% (Fig. 2D). The melting temperature of the stoichiometric $CuSbSe_2$ is 481 ± 3 °C. Temperature values were measured using differential thermal analysis.

According to [19], Cu_3SbSe_3, $CuSbSe_2$, and $Cu_{10.53}Sb_{33.78}Se_{55.68}$ ternary compounds are formed in the $Cu_{2-X}Se$-Sb_2Se_3 system. Their cell parameters and space groups (SG), reported in the papers [41–46], are summarized in the Table 2.

For the high-temperature phase $Cu_{10.53}Sb_{33.78}Se_{55.68}$, no structural data were documented. Its existence range was tentatively defined from 450 to 500 °C [19].

Documenting the results of the studies of the Cu_2Se and Sb_2Se_3-based solid solution, Karup-Moller did not report either direct experimental data on the variations in unit cell parameters, or the data

Table 2
Unit cell parameters and symmetry of the ternary compounds in the $Cu_{2-X}Se$-Sb_2Se_3 system.

Ref.	SG, crystal system	Z	ST	Unit cell parameters			
				a, (Å)	*b*, (Å)	*c*, (Å)	*V*, (Å^3)
$CuSbSe_2$							
[41]	*Pnma*, orthorhombic	4	$CuBiS_2$	6.40	3.95	15.33	387.54
[42]				6.299(2)	3.9734(12)	15.005(5)	375.5(2)
[43]				6.302	3.988	14.957	375.9
[44]				6.2988(8)	3.981(5)	15.003(2)	376.21(8)
Cu_3SbSe_3							
[45]	*Pnma*, orthorhombic	4	Cu_3SbSe_3	7.959(1)	10.583(1)	6.824(1)	574.79
[46]				7.9865(8)	10.6138(9)	6.8372(7)	579.6(1)

from the thermoanalytical experiments, and microstructure studying [19].

There was no information on the enthalpies of phase transformations in the Cu_2Se-Sb_2Se_3 system, and no relevant thermodynamic calculations [19,39,40,47].

It is not explained in [47] why compounds Cu_3SbSe_3 and $CuSbSe_2$ with different chemical compositions and structures have coinciding microhardness values. The phase composition of the sample containing 75 mol% Sb_2Se_3 at elevated temperatures, features of thermal expansion of equilibrium phases, which can qualitatively explain the reasons for their interaction, have not been determined. Papers [39,40] do not present the data of thermal analysis, the results of studying the microstructure and phase composition of the samples.

It is an efficient strategy to combine differential scanning calorimetry with liquidus calculations by the Redlich-Kister equation [48]; along with other models [49–51]; this method has been actively developed in recent years [52–55].

In this work, we sought to determine the structure and properties of ternary phases formed in the $Cu_{2-X}Se$-Sb_2Se_3 system, to obtain the phase diagram of the $Cu_{2-X}Se$-Sb_2Se_3 system, to find balance equations for phase transformations, and to calculate the liquidus using the Redlich-Kister equation.

2. Experimental details

2.1. Synthesis

The samples of $Cu_{2-X}Se$ and Sb_2Se_3 binary compounds and $Cu_{2-X}Se$-Sb_2Se_3 samples (from 3 to 7 g) were prepared from elements: antimony (99.9999 wt%), selenium (> 99.997 wt%), and electrolytic copper (99.99 wt%, purchased from Khimreaktiv, Russia). The weight of the synthesized samples ranged from 3 to 7 g. The accuracy of weighting the starting reactants is ± 0.00005 g (via a Mettler Toledo ME204 analytical balance). The reactants were placed into the optical silica glass ampoules (with volumes up to 5 cm^3). The ampoules were degassed to 0.1 Pa and then sealed off [56]. Heat treatment mode for the reactants placed in degassed and sealed silica glass ampoules has been developed according to the data reported in the papers [19,39,40,47,57]. The ampoules with the samples were heated at 50–100 °C/day until the entire sample melted (depending on the sample, the melting temperature varied from 500 to 1150 °C, i.e. the whole heating procedure took from 120 to 300 h). The molten samples were kept at these temperatures for 1 h with the ampoules intermittently manually vibrated using a special home-made device [57–60]. Then the melts were either cooled at 50–100 °C/h or quenched in water at 20 °C. Samples containing 25 and 50 mol% Sb_2Se_3 were also prepared by the ceramic method. Preliminary synthesized binary compounds copper selenide and Sb_2Se_3 were weighted and then pressed into cylinders at 196 MPa. The ampoules with samples were annealed at 350 °C 750 h, at 350 °C 1100 h, at 470 °C 1950 h, and at 450 °C for 4300 h, at 480 °C for 4300 h. The temperature in the muffle furnaces was maintained with an accuracy of ± 5 °C and automatically restored in case of power supply failures.

2.2. The ratio of elementary substances Cu, Sb, Se for the studied samples, the phase composition of the samples after synthesis and annealing

Due to the fact that the $Cu_{2-X}Se$ phase acquires a copper-deficient nonstoichiometry during synthesis, we studied the $Cu_{2-X}Se$-Sb_2Se_3 and $Cu_{2-X}Se$-Cu_3SbSe_3 systems for various ratios of copper and selenium. In the present paper, the samples of copper semiselenide, which were synthesized and studied, are indicated not by lower case indices, but by the atomic ratio of the elements of copper and selenium, placed in a quartz ampoule. The weighted portions of elementary substances, which were placed in quartz ampoules, were calculated for the following sample compositions: section I: (1-X) × (2.000 Cu: 1.000 Se) + X Sb_2Se_3 (X = 0–1.0); section II: (1-X) × (1.995 Cu: 1.000 Se) + X Cu_3SbSe_3; section III: (1-X) × (1.990 Cu: 1.000 Se) + X Cu_3SbSe_3 (X = 0–1.0); section IV: (1-X) × (1.970 Cu: 1.000 Se) + X Cu_3SbSe_3 (X = 0–1.0); section V: (1-X) × (1.950 Cu: 1.000 Se) + X Cu_3SbSe_3 (X = 0–1.0); section VI: (1-X) × (1.930 Cu: 1.000 Se) + X Cu_3SbSe_3 (X = 0–1.0).

When studying the section Cu_2Se-Sb_2Se_3, in the range of compositions 25–100 mol% Sb_2Se_3, conforming results of physicochemical studies were obtained for several series of samples. Impurity phases were present only in single synthesized and annealed samples. The results of the physicochemical study of samples from the Cu_2Se-Sb_2Se_3 section for the concentration range 25–100 mol% Sb_2Se_3 are plotted on the diagram of the $Cu_{2-X}Se$-Sb_2Se_3 system.

In the concentration range 0–25 mol% Sb_2Se_3 system $Cu_{2-X}Se$-Cu_3SbSe_3 was studied in six sections (I-VI). In each section, from 2 to 15 samples were synthesized. We tried to determine the composition of copper selenide, which is in equilibrium with the Cu_3SbSe_3 phase, in order to present the phase diagram of the $Cu_{2-X}Se$-Sb_2Se_3 system without phase equilibrium lines from the ternary system Cu-Sb-Se [61–63].

3. Methods of physicochemical analysis

Microstructural analysis (MSA) was carried out on AxioVert.A1MAT metallurgical microscope (0.5 µm resolution). The AxioVision SE64 program suite was used to calculate the amount of grains of different phases [61]. In order to get clear photographs, thin polished sections of the samples were etched with chromosulfuric acid. The chemical and grain compositions of the samples as well as particle morphology were determined at three sites on the surface of the sample by scanning electron microscopy (SEM) using a Tescan Mira 3 LMU scanning electron microscope (SEM) equipped with an energy dispersive X-ray spectroscopy (EDS) Oxford instruments unit (with references) and INCA analyzer software [64]. EDS data were used to map the surface distributions of elements in Aztec software.

Microhardness [65] was measured using an HMV-G21DT microhardness tester using HMV-G data processing software [60]. The result represented an average value over 15 clear-cut indents.

Samples for metallographic studies and microhardness measurements were embedded into the epoxy resin, ground with alumina abrasive papers (P180-P1000), polished with chromium(III) oxide (0.3 µm) paste and diamond (0.1/0 µm) paste, cleaned with ethanol, and then cotton swab dried. For SEM characterization, samples were prepared in a similar way but without embedding in epoxy resin [60,66–69].

Standard calculation software was used in calculations with using Redlich-Kister equation [70].

The phase diagrams for this paper were plotted using software edstate23D developed in Tyumen state university, including computer programs edstate2D (to calculate the binary phase diagrams) and edstate3D (to plot flat isothermal sections of the ternary phase diagrams) [71].

The DSC data for each group of the experimental points of the phase diagram of the $Cu_{2-X}Se$-Sb_2Se_3 system were approximated by a third-order polynomial using the edstate2D program, entering the invariant points as compulsory. The same edstate2D program was used to reproduce the documented binary phase diagrams in the ternary Cu-Sb-Se system. The program edstate3D was used to plot the isothermal section of the ternary Cu-Sb-Se system at 20 °C.

Differential scanning calorimetry (DSC) experiments [66] were carried out on a Setsys Evolution 1750 (TGA–DSC 1600) thermal analyzer with a Pt/PtRh (10%) thermocouple using SETSOFT 2000 data processing software, and on a STA 449 F3 Jupiter simultaneous thermal analyzer with a W3%Re-W25% thermocouple using NETZSCH Proteus 6.1 software. The heating rate was 3 or 5 °C/min [67]. Samples for DSC (100–110 mg) were placed into quartz ampoules (about 100 µL), which were then sealed off. A sealed-off empty ampoule served as a reference [72]. For calibration, pure metal standards: In (99.9995%), Sn (99.9995%), Bi (99.9995%), Al (99.995%), Zn (99.995%), Ag (99.999%), Au (99.9995%), Pb (99.9995%), Cu (99.999%), Pd (99.999%) were used. The Setsys Evolution 1750 (TGA–DSC 1600) has a measurement error of ± 1.8 °C in determining the temperature and 11.6% in determining the enthalpies of phase transitions. The STA 449 F3 Jupiter has a measurement error of ± 1.50 °C in determining the temperature and 6.9% in determining the enthalpies of phase transitions [66].

X-ray powder diffraction (XRD) patterns were recorded on DRON-7 [66–68] (Ni-filtered CuK_{α} radiation (λ = 1.5406 Å)), on Bruker D2 Phaser [73] (Ni-filtered CuK_{α} radiation (λ = 1.5406 Å)), and on Rigaku Ultima IV (CuK_{α} radiation (λ = 1.5406 Å), Graphite monochromator Cu (Flexible)) [74] diffractometers. The following software was used: PDWin 4.0 [66–68], Topas 6 [75], Bruker Diffrac.EVA [73], and HighScore version 3.0 (2012) with reference to the PDF-2 File and Crystallography Open Database (COD) [76]. The samples were further studied at a D8 Advance Bruker X-ray diffractometer equipped with an HTK-1200 N Anton Paar high-temperature chamber in the temperature range 20–480 °C using CuKα radiation [75]. High-temperature powder X-ray diffraction (HTXRD) experiments were carried out at 100, 200, 300, 400, 410, 420, 430, 440, 450, 460, 470, and 480 °C. The sample was put into a high-temperature chamber with Pt heating filament. If the sample amount was small, X-ray radiation penetrated Pt heating filament. The intensity of the platinum line served to assess the degree of sublimation of sample during experiment. The platinum percentage at 20 °C was 4.3 mol% Pt. Unit cell parameters of the phases for each temperature were calculated using the FULLProf software package [77]. The X-ray diffraction patterns were processed by the Rietveld method [78] in the Topas 6 program [79,80]. Thermal expansion was determined for $CuSbSe_2$ and Sb_2Se_3 selenides from powder HTXRD data. Eigenvalues of thermal expansion tensor were determined using the polynomial approximation of temperature dependencies of the unit-cell parameters by the Theta To Tensor & Rietveld To Tensor software [81,82].

Single-crystal X-ray diffraction data for $CuSbSe_2$ and Cu_3SbSe_3 were collected at an Oxford Diffraction Gemini R Ultra X-ray diffractometer equipped with a CCD area detector using MoKα radiation [83]. For these studies we used the fragments of the broken polycrystalline blocks that were solidified by slow cooling of melt, and then annealed. They contained several differently oriented single-crystalline domains. CrysAlisPro software [84] was used for data collection, unit cell determination, and primary data processing. The structures were solved using the dual-space algorithm implemented in SHELXT software [85]. Refinement was done using SHELXL-2018 [86] with ShelXle [87] as the GUI. IUCr Checkcif/PLATON service [88] was used to validate the structural model. VESTA [89] was used for graphical representation of the crystal structures. The complete structural data set was deposited with the CSD [90] (refcodes CCDC 2080025–2080026).

Diffuse reflectance spectra were taken from thin layers of powders in the range 200–1400 nm using a UV-2600 Shimadzu (Japan) spectrophotometer equipped with an ISR-2600Plus integrating sphere attachment [91]. $BaSO_4$ standard supplied by Shimadzu with the spectrophotometer was used in the measurement of diffuse reflection spectra. Upon building the linear fit for the fundamental absorption region, we chose the regions of linearity in the way that enabled Pearson correlation coefficient to be 0.999 just like, e.g., in the paper by Rampino [92].

4. Results and discussion

4.1. The samples of ternary compounds Cu_3SbSe_3 and $CuSbSe_2$ of the $Cu_{2-X}Se$-Sb_2Se_3 system

The polycrystalline samples of ternary compounds (Cu_3SbSe_3 and $CuSbSe_2$) of the $Cu_{2-X}Se$-Sb_2Se_3 system that were prepared from elements and annealed at 450 °C for 4300 h, were analyzed by several instrumental techniques. The part of the sample used for analyzing by X-ray powder diffraction and for particle morphology characterization by scanning electron microscopy was preliminary fine-ground manually in a mortar. The part of the sample used for elemental analysis using the same scanning electron microscope (see Experimental details) was studied after surface polishing.

X-ray powder diffraction patterns of the samples of Cu_3SbSe_3 and $CuSbSe_2$ ternary compounds of the $Cu_{2-X}Se$-Sb_2Se_3 system that were prepared from elements and annealed at 450 °C for 4300 h are shown in Fig. 3.

According to the X-ray powder diffraction analysis, the samples of the ternary compounds contained a single phase each. Therefore, we decided to study the samples by several instrumental techniques.

The crystallites of Cu_3SbSe_3 in the thin polished sections of the cooled molten polycrystalline samples were of light gray color with a faint greenish tint. The crystallites of $CuSbSe_2$ in the polished thin sections were light-colored with a grayish tint. In the $Cu_{2-X}Se$-Sb_2Se_3 system, the microhardness of the phases changes completely regularly: $Cu_{2-X}Se$ H = 99 ± 7 HV, Cu_3SbSe_3 H = 235 ± 5 HV, $CuSbSe_2$ H = 179 ± 9 HV, Sb_2Se_3 H = 45 ± 3 HV.

The SEM images of the particles and the element distribution of the samples of Cu_3SbSe_3 and $CuSbSe_2$ ternary compounds are shown in Fig. 4.

The crystallites in Cu_3SbSe_3 had the sizes of about 5–30 µm and a dense grain structure. Most $CuSbSe_2$ grains had a layered structure. The layer thickness was 0.1–0.3 µm. The crystallites of the compounds had polyhedral shapes with the angles of 60° and 120° (Fig. 4).

The distribution of copper, antimony, and selenium in the thin polished sections of the solid samples, as probed by SEM, was uniform in full agreement with XRD data (Fig. 4). EDS elemental

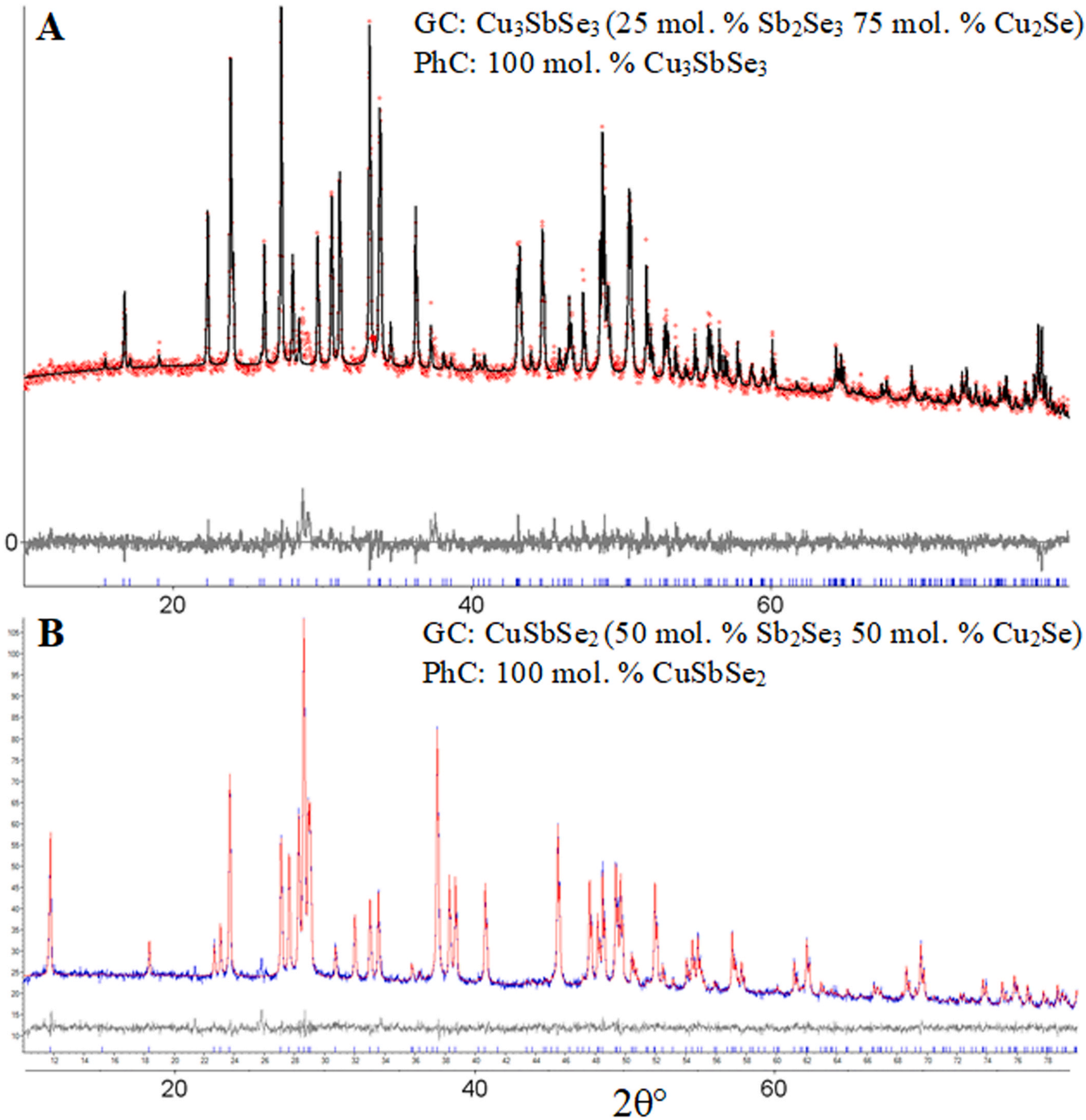

Fig. 3. X-ray diffraction patterns of the samples of ternary compounds of the $Cu_{2-x}Se$-Sb_2Se_3 system annealed at 450 °C for 4300 h: (A) Cu_3SbSe_3 and (B) $CuSbSe_2$. Experimental patterns, calculated diffraction patterns, difference plot and the positions of diffraction patterns in the calculated patterns.

mapping made it possible to identify also the traces of minor phases. Thus, in the Cu_3SbSe_3 sample, there were a few selenium-enriched grains. In the $CuSbSe_2$ sample, there was one antimony grain smaller than 10 µm.

The fragments of sub-millimeter sizes were separated from the polycrystalline Cu_3SbSe_3 and $CuSbSe_2$ samples and studied by single-crystal X-ray diffraction. For the first time, the crystal structure of Cu_3SbSe_3 and $CuSbSe_2$ compounds on single-crystal blocks was studied. Unfortunately, we failed to break blocks so that to get true single-crystal samples. The blocks contained several single-crystalline fragments. However, most reflections from a multi-crystalline sample did not overlap, so that the crystal structure refinement provided acceptable and reliable results. The data collection and refinement details as well as crystal data are summarized in Electronic supplementary information (ESI) (Table S1).

The fragments of the Cu_3SbSe_3 and $CuSbSe_2$ crystal structures were obtained (refcodes CCDC 2080025–2080026). The $CuSbSe_2$ structure is built of $SbSe_5$ square pyramids and $CuSe_4$ tetrahedra

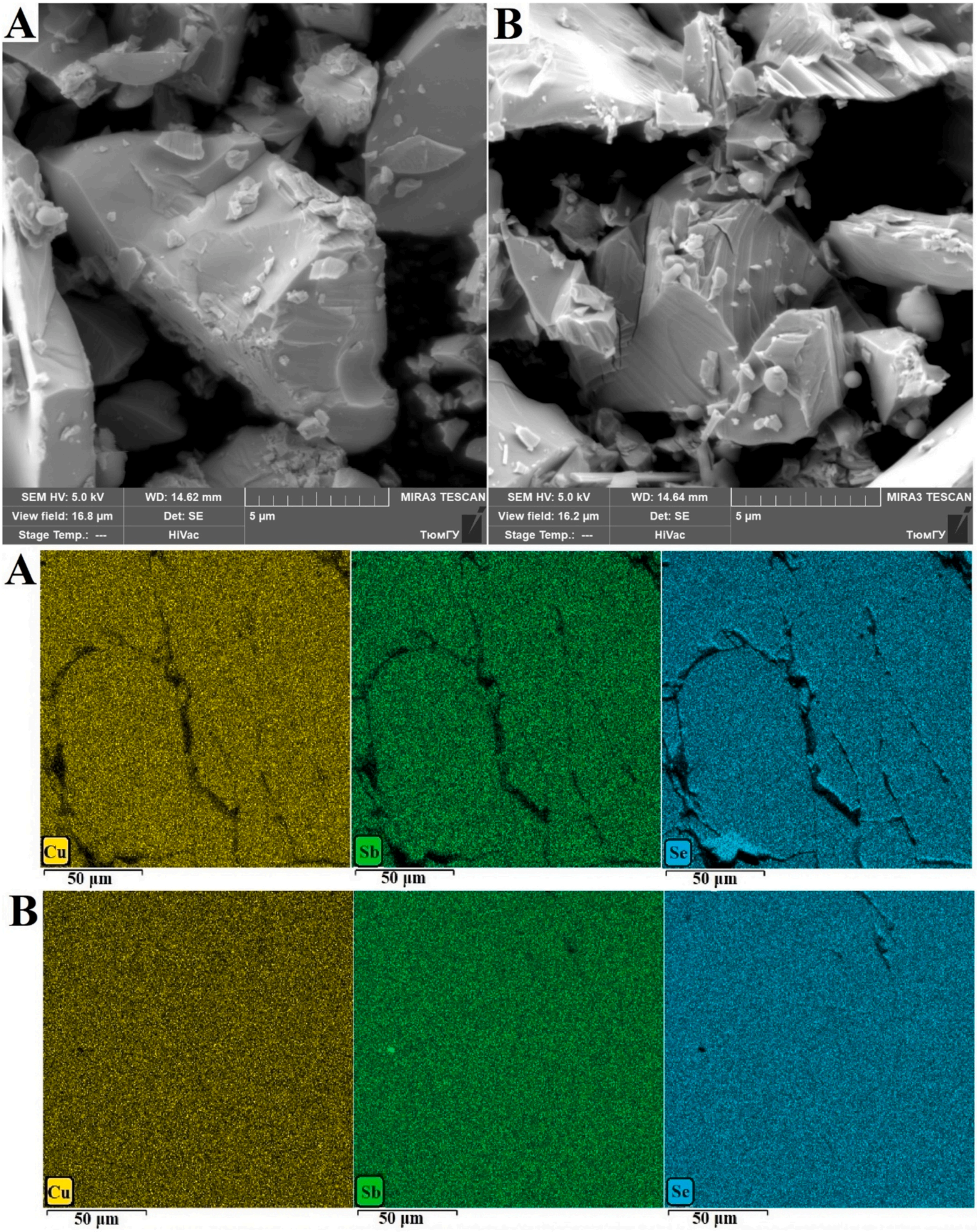

Fig. 4. SEM images of particles of powders and EDS elemental mapping showing the distribution of chemical elements Cu, Sb, Se in thin polished sections for samples of ternary compounds: A – Cu_3SbSe_3. B – $CuSbSe_2$.

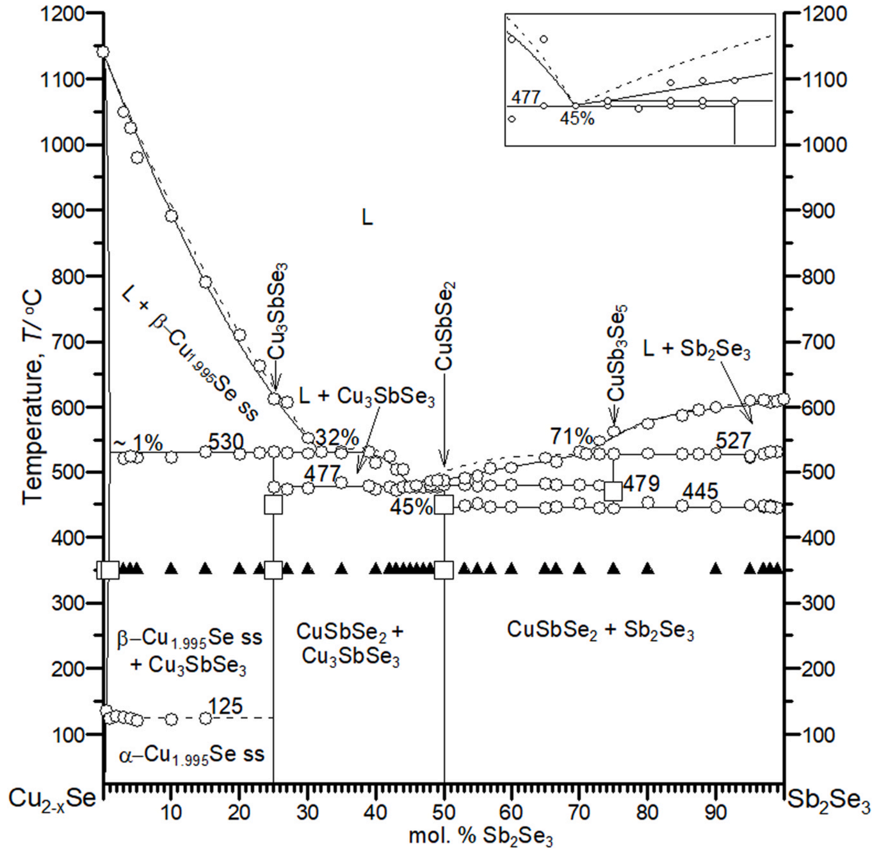

Fig. 5. $Cu_{2-x}Se$–Sb_2Se_3 phase diagram. Notations: ○ DSC data, □ single-phase and ▲ two-phase samples according to XRD and MSA. Solid lines are experimental data; dashed lines show the calculation results based on the Redlich-Kister equation.

forming a three-dimensional network, in agreement with the previously published data [93]. The Cu_3SbSe_3 crystal structure is built of $CuSe_4$ tetrahedra and $SbSe_3$ distorted triangles forming a three-dimensional network, also in agreement with the previously published data [46].

The bandgap of a semiconductor is an important characteristic that influences possible applications. The bandgaps of $CuSbSe_2$ and Cu_3SbSe_3 were determined from the diffuse reflectance spectra taken from thin layers of powders in the range 200–1400 nm via the Kubelka-Munk function [94] (Electronic supplementary information (ESI), Fig. S1).

The bandgaps of both materials are close to 1 eV: direct E_g = 1.1 eV for $CuSbSe_2$, and indirect E_g = 0.963 eV for Cu_3SbSe_3. These values are in fair agreement with previously reported measurements. Rampino et al. [92] reported direct E_g = 1.11 eV for stoichiometric $CuSbSe_2$ and indirect E_g = 0.95 eV for copper-deficient $CuSbSe_2$. Wei et al. [95] reported indirect E_g = 0.95 eV for Cu_3SbSe_3. For the first time, the optical band gap of compounds was determined on single-phase samples of stoichiometric compositions.

4.2. Phase equilibria in the $Cu_{2-x}Se$–Sb_2Se_3 system. The $Cu_{2-x}Se$–Sb_2Se_3 phase diagram

The $Cu_{2-x}Se$-Sb_2Se_3 phase diagram was plotted over the entire range of concentrations from 25 °C to complete melting of all alloys (Fig. 5). Six phase transformations altogether take place in the system (Table 3).

Cu_3SbSe_3 and $CuSbSe_2$ are incongruently melting compounds. Their melting peaks on heating curves have well-defined linear segments (Fig. 6; samples (1) and (4)), in agreement with the invariant phase equilibrium of the decomposition of compounds.

Cooling curves give evidence of the exothermal effects. For a 25 mol% Sb_2Se_3 sample, these are the Cu_3SbSe_3 crystallization peak and the peak corresponding to the "$1Cu_3SbSe_3 + 8 CuSbSe_2$" eutectic crystallization. In a 50 mol% Sb_2Se_3 sample, the two peaks correspond to the crystallization of $CuSb_3Se_5$ primary crystals and $CuSbSe_2$.

The heat effects corresponding to the incongruent melting of the ternary compounds were observed in the following composition ranges: for Cu_3SbSe_3, from 1.5 to 32 mol% Sb_2Se_3, and for $CuSbSe_2$, from 48 to 75 mol% Sb_2Se_3. The Tamman triangle plotted for the enthalpies of melting of the compounds unambiguously indicates that the observed thermal features are related to the melting of the ternary compounds.

Balance equations were calculated for the incongruent melting of Cu_3SbSe_3 and $CuSbSe_2$; the heats of the transformations were determined by DSC (Table 3, Fig. 6).

In the concentration range 25–50 mol% Sb_2Se_3 in the crystalline state, the Cu_3SbSe_3 and $CuSbSe_2$ phases are in equilibrium. On the X-ray diffraction patterns of annealed samples, there are only diffraction peaks of conjugated phases (Fig. 7). Cu_3SbSe_3 and $CuSbSe_2$ form eutectic mixtures. The peak of the thermal effect of eutectic melting is present in the DSC curves of all two-phase samples and manifests itself at a temperature of 477 °C (Fig. 6, samples (2), (3), (4)). The apex of the Tammann triangle of eutectic melting enthalpies falls on the composition of 45 mol% Sb_2Se_3 (Fig. 6, sample (3)).

On the DSC curve of a sample of this composition, there is the only peak of melting of eutectic crystals (Fig. 6, sample (3)). The samples were also studied by SEM (Fig. 8). According to two independent research methods based on different physical principles, the composition of the eutectic is taken as (45 ± 1) mol% Sb_2Se_3. Since the constituent eutectic phases are Cu_3SbSe_3 and $CuSbSe_2$, it

Table 3
Balance equations of invariant equilibria in the $Cu_{2-x}Se$-Sb_2Se_3 system.

No.	Phase transformation	Invariant point coordinates		Phase transformation equation, mol%	ΔH, J/g	ΔH, kJ/mol
		composition, mol% Sb_2Se_3	T/°C			
1	Incongruent melting of Cu_3SbSe_3	25	530	Cu_3SbSe_3 (0.25 Sb_2Se_3; 0.75 $Cu_{1.995}Se$) ↔ 0.226 β-$Cu_{1.995}Se$ ss (0.01 Sb_2Se_3; 0.99 $Cu_{1.995}Se$) + 0.774 L (0.32 Sb_2Se_3; 0.68 $Cu_{1.995}Se$)	67.6	37.1
2	Eutectic (1Cu_3SbSe_3 + 8$CuSbSe_2$) melting	45	477	0.889 $CuSbSe_2$ (0.5 Sb_2Se_3; 0.5 $Cu_{1.995}Se$) + 0.111 Cu_3SbSe_3 (0.25 Sb_2Se_3; 0.75 $Cu_{1.995}Se$) ↔ L(0.45 Sb_2Se_3; 0.55 $Cu_{1.995}Se$)	73.3	–
3	Incongruent melting of $CuSbSe_2$	50	479	$CuSbSe_2$ (0.5 Sb_2Se_3; 0.5 $Cu_{1.995}Se$) ↔ 0.862 L(0.46 Sb_2Se_3; 0.54 $Cu_{1.995}Se$) + 0.138$CuSb_3Se_5$ (0.75 Sb_2Se_3; 0.25 $Cu_{1.995}Se$)	85.1	29.2
4	Formation of high-temperature compound $CuSb_3Se_5$	75	445	0.500Sb_2Se_3 + 0.500$CuSbSe_2$ (0.5 Sb_2Se_3; 0.5 $Cu_{1.995}Se$) ↔ $CuSb_3Se_5$ (0.75 Sb_2Se_3; 0.25 $Cu_{1.995}Se$)	21.5	17.7
5	Incongruent melting of $CuSb_3Se_5$	75	527	$CuSb_3Se_5$(0.75 Sb_2Se_3; 0.25 $Cu_{1.995}Se$) ↔ 0.138Sb_2Se_3 + 0.862 L (0.71 Sb_2Se_3; 0.29 $Cu_{1.995}Se$)	36.7	30.2
6	Eutectoid phase transformation in $Cu_{2-x}Se$ ss	1	125	0.020 Cu_3SbSe_3(0.25 Sb_2Se_3; 0.75 $Cu_{1.995}Se$) + 0.980 α-$Cu_{1.995}Se$ ss (0.005 Sb_2Se_3; 0.995 $Cu_{1.995}Se$) ↔ β-$Cu_{1.995}Se$ ss (0.01 Sb_2Se_3; 0.99 $Cu_{1.995}Se$)	11	2.3

seems appropriate to write the eutectic composition as (1Cu_3SbSe_3 + 8$CuSbSe_2$).

Eutectic mixtures consisted of extended oval grains of Cu_3SbSe_3 and $CuSbSe_2$ phases, 1.5–4 µm wide and an average length of 5–9 µm, located in the volume of $CuSbSe_2$ phase crystals of almost the same dimensions, a width of 2–5 µm, and a length of 4–11 µm (Fig. 8, sample B).

The Cu_3SbSe_3 and $CuSbSe_2$ primary crystals as crystallized from the melt had different shapes. The Cu_3SbSe_3 primary crystals were typically oval with linear sizes of 25–250 µm and angles of 120°. The $CuSbSe_2$ primary crystals were oblong, 10–50 µm wide and 100–350 µm long. In some areas of the sample, crystals formed layered structures. Eutectic crystals were located in the interlayers in-between the layered oblong primary crystals of $CuSbSe_2$ (Fig. 8).

In the concentration range 50–100 mol.% Sb_2Se_3, a high-temperature compound of provisional composition $CuSb_3Se_5$ was formed. The endotherm due to the formation of this compound appeared at 445 °C in all the samples that contained more than 50 mol.% Sb_2Se_3.

Several methods were used to prepare 75 mol% Sb_2Se_3 samples, in particular, by careful co-grinding of the powder samples of the annealed $CuSbSe_2$ and Sb_2Se_3 compounds. The formation of phases in particles during grinding of layers, a decrease in particle size to 0.5–2 µm, form a high specific surface of phase contact. Such an approach is known to be efficient in the solid-state inorganic synthesis. The authors of papers [96–101] used mechanochemistry methods to increase the chemical activity of reagents. The mechanical treatment of $CuSbSe_2$ and Sb_2Se_3 phases yields the high-temperature phase $CuSb_3Se_5$ already on the first heating of the sample to 450 °C [38].

The DSC curve of the sample 6 in Fig. 6 features a peak due to $CuSb_3Se_5$ phase formation at 445 °C (ΔH = 21.5 J/g) and then a weak peak at 479 °C due to the incongruent melting of $CuSbSe_2$ (ΔH = 1.92 J/g). The enthalpy of $CuSbSe_2$ melting in a 75 mol% Sb_2Se_3 sample calculated on the assumption of the absence of the $CuSb_3Se_5$ phase in the system ΔH = 0.5 × 145 = 72.5 J/g. The DSC data were used to calculate the yield of reaction (4) in a sample heated to 500 °C as 100% - (1.92 J/g: 72.5 J/g) × 100% = 97.35%. The yields of the reaction (4) for several independently prepared samples ranged within 90–97.5%. The values of the enthalpies for reactions (4) and (5) are given in Table 3. According to the DSC data, the transformation completeness for the reaction (4) was equal to 97%.

The average temperature of $CuSb_3Se_5$ incongruent melting is 527 °C for the samples whose compositions lie in the range 72–99 mol% Sb_2Se_3. In the paper [102] proposed a technique for separating the areas of overlapping peaks originating from various thermal effects. The overlapping peaks due to the melting of $CuSb_3Se_5$ (36.7 J/g) and the melting of Sb_2Se_3 primary crystals (29.6 J/g) (Fig. 6: samples (6), (7)) were resolved as described in the paper [102]. The temperatures and enthalpies of $CuSb_3Se_5$ decomposition were reproduced in parallel experiments. Tammann triangle plotting shows that the thermal events have the highest values at 75 mol% Sb_2Se_3. When the samples were heated further after the $CuSb_3Se_5$ decomposition, the DSC curves featured the melting of the Sb_2Se_3 crystals. The end temperatures of these thermal events were identified as liquidus temperatures (Fig. 6: samples (6) and (7)).

During the cooling of the sample 75 mol% Sb_2Se_3 two sets of undercooling thermal events were recorded. As a rule, Sb_2Se_3 and $CuSb_3Se_5$ grains crystallize simultaneously following the reaction (4). The decomposition of $CuSb_3Se_5$ and the formation of $CuSbSe_2$ by reaction (5) also occurred in close temperature ranges, or simultaneously (Table 3).

The high-temperature phase $CuSb_3Se_5$ was not detected upon cooling or quenching. $CuSbSe_2$ and Sb_2Se_3 were the equilibrium phases at temperatures below 445 °C in the range 50–100 mol%

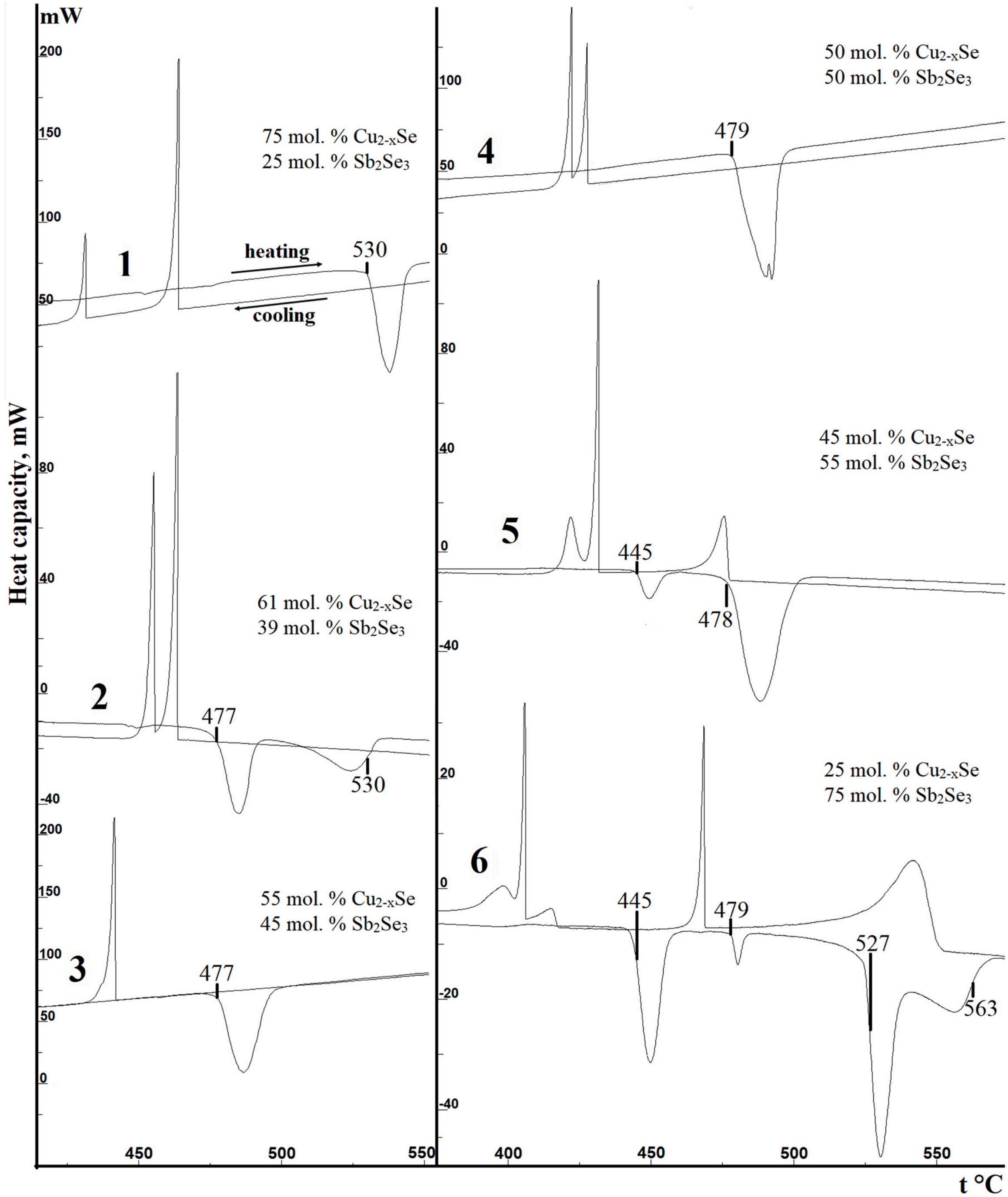

Fig. 6. DSC traces for $Cu_{2-x}Se$-Sb_2Se_3 samples containing: (1) 25.0, (2) 39.0, (3) 45.0, (4) 50.0, (5) 55.0, and (6) 75.0 mol% Sb_2Se_3.

Sb_2Se_3. The compositions of the samples in this range did not change during annealing for 750 and 1100 h at 350 °C (Fig. 8: sample D). Sample 75 mol% Sb_2Se_3 was studied by high-temperature powder X-ray diffraction (Fig. 9). Weak reflections from the platinum heating filament were detected at 20 °C (Fig. 9A).

The intensity of the platinum lines was used to estimate the degree of sublimation of the sample during experiment. The systematic increase in the intensity of platinum reflections in the diffraction patterns collected on heating was indicative of sublimation of the selenides. At 20 °C, the sample consists of the $CuSbSe_2$ and Sb_2Se_3 phases, the reflection of platinum is also fixed. The platinum percentage at 20 °C was 4.3 mol% Pt (Fig. 9A).

Sublimation of the selenides in the diffractometer chamber became visually observable at 450 °C. At 480 °C, the percentage of the platinum in the sample including the substrate and the selenides was as high as 25.54 mol% Pt (Fig. 9B).

5. Thermal expansion of $CuSbSe_2$ and Sb_2Se_3

As temperature rises, the unit cell parameters of $CuSbSe_2$ and Sb_2Se_3 phases increase continuously up to 460 °C (Fig. 10). The temperature dependencies of the unit-cell parameters were approximated by quadratic polynomial functions $p_T = p_0 + p_1T + p_2T^2$ where p_T denotes *a*, *b*, *c* and *V* parameters for both selenides within

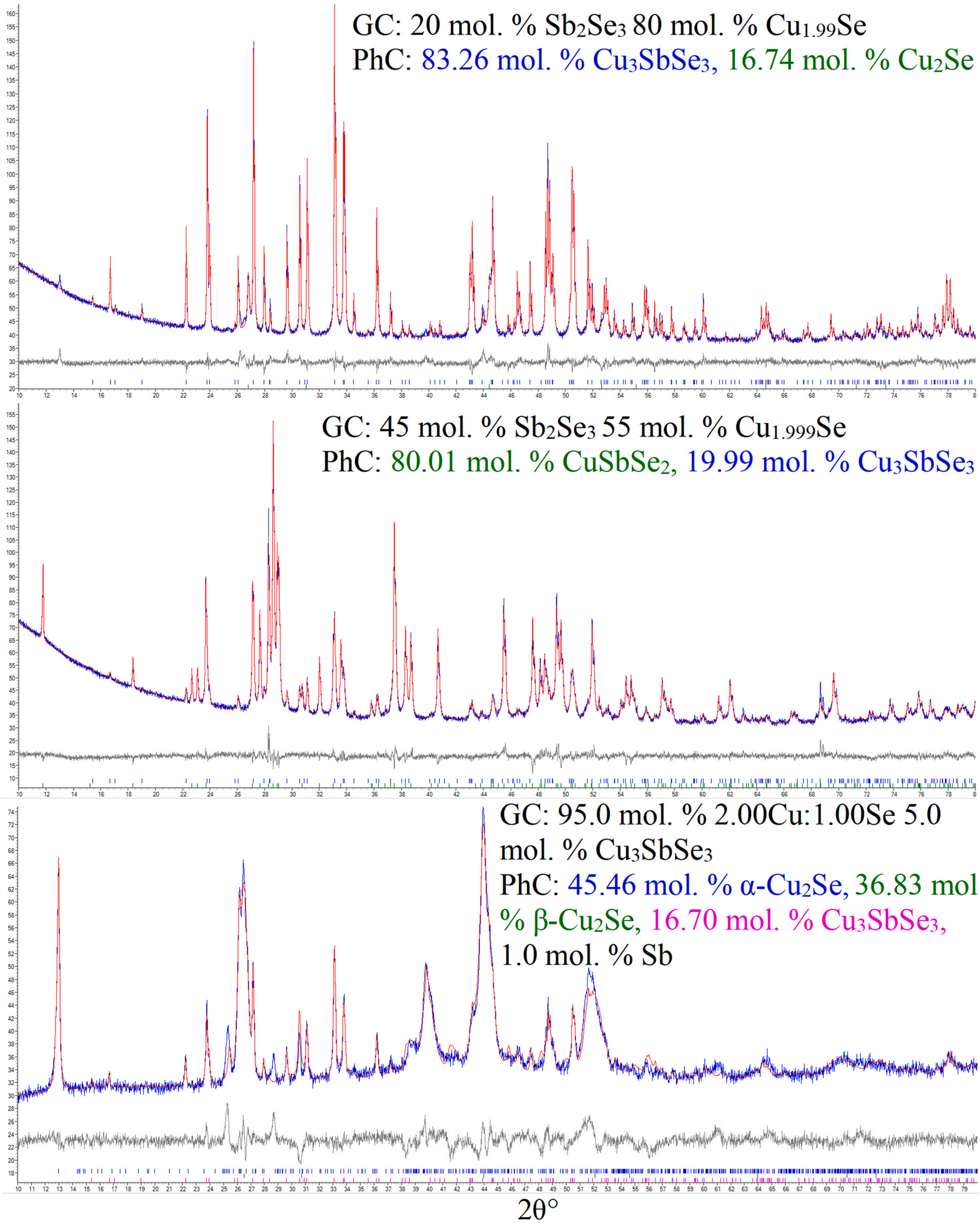

Fig. 7. X-ray diffraction patterns of annealed at 350 °C during 750 h samples. Notations: GC – as-batch (global) composition; PhC - phase composition of the sample.

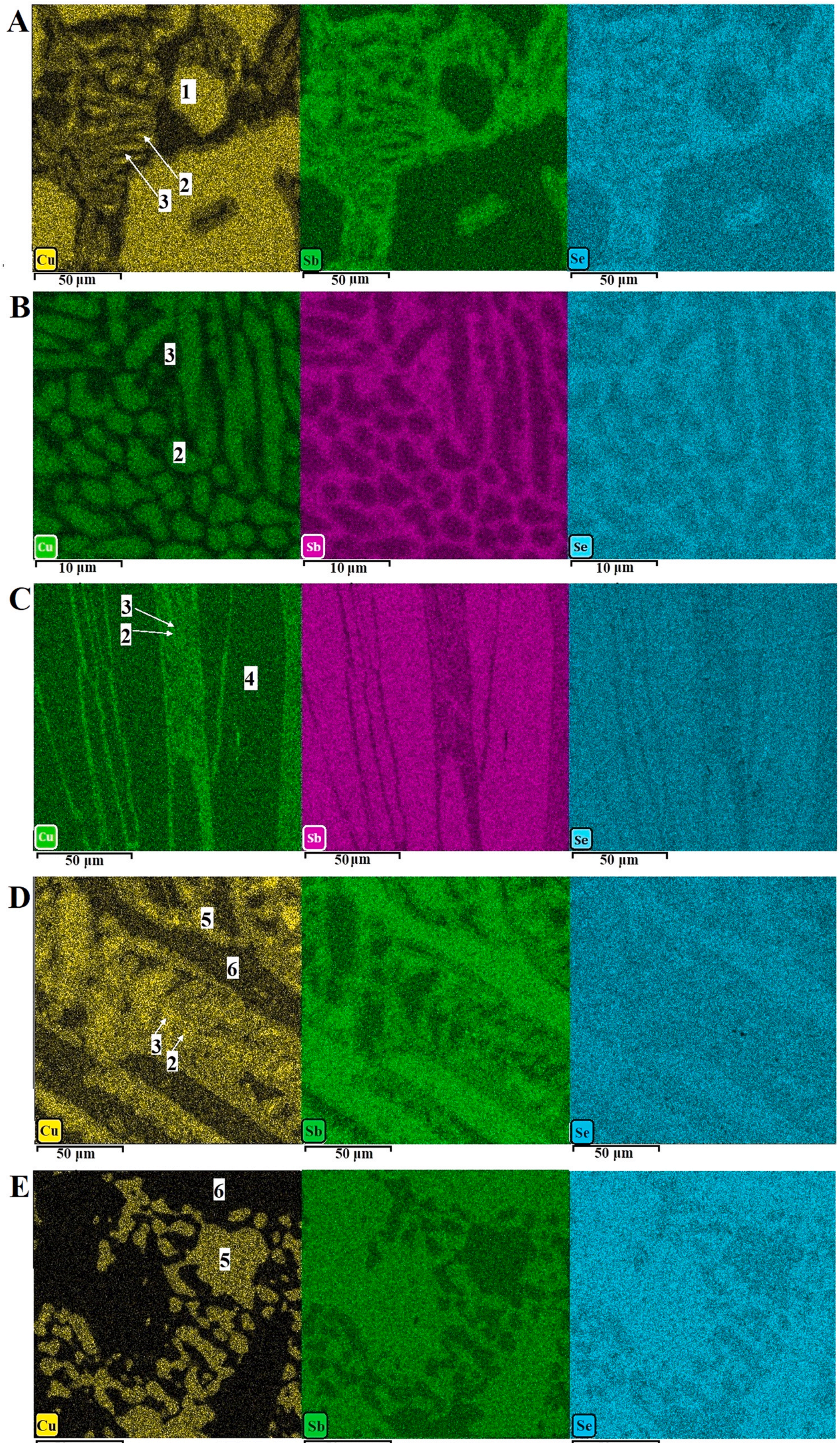

Fig. 8. SEM images illustrating the Cu, Sb, and Se concentrations in polished thin sections of heat-treated samples of as-batch composition (mol% Sb_2Se_3): (A) 39.0, (B) 45.0, (C) 48.0, (D) 55.0, and (E) 75.0. (1, 2) Cu_3SbSe_3 grains: (1) primary grains crystallized from the melt and (2) eutectic grains. (3, 4, 5) $CuSbSe_2$ grains: (3) eutectic, (4) primary, and (5) having compositions in the range 50–100 mol% Sb_2Se_3. (6) Sb_2Se_3 grains.

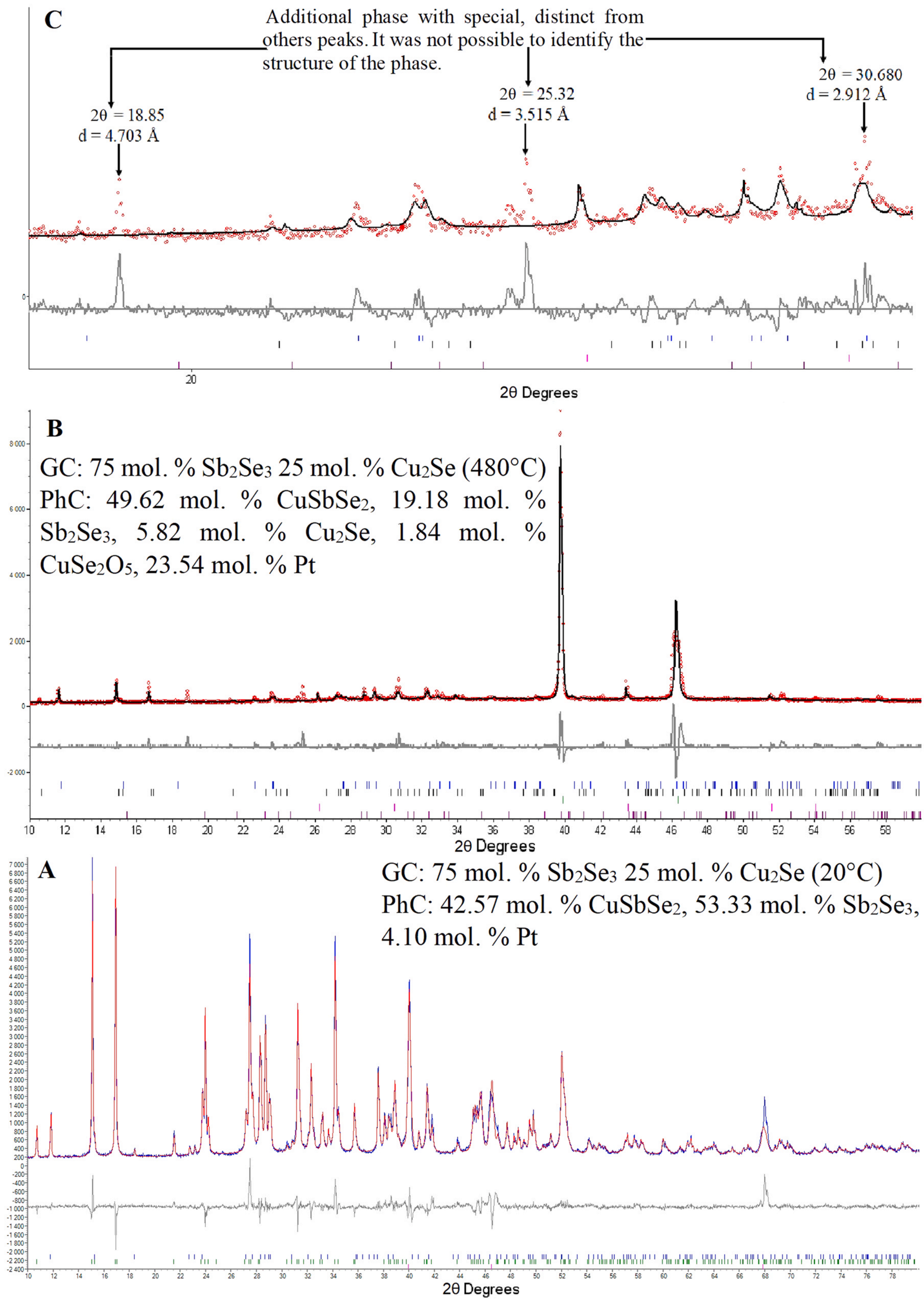

Fig. 9. X-ray diffraction patterns of a 75 mol% Sb_2Se_3 + 25 mol% Cu_2Se sample at (A) 20 °C and (B) 480 °C; and (C) a fragment of the 480 °C X-ray diffraction pattern where the peaks of the newly formed $CuSb_3Se_5$ phase are indicated.

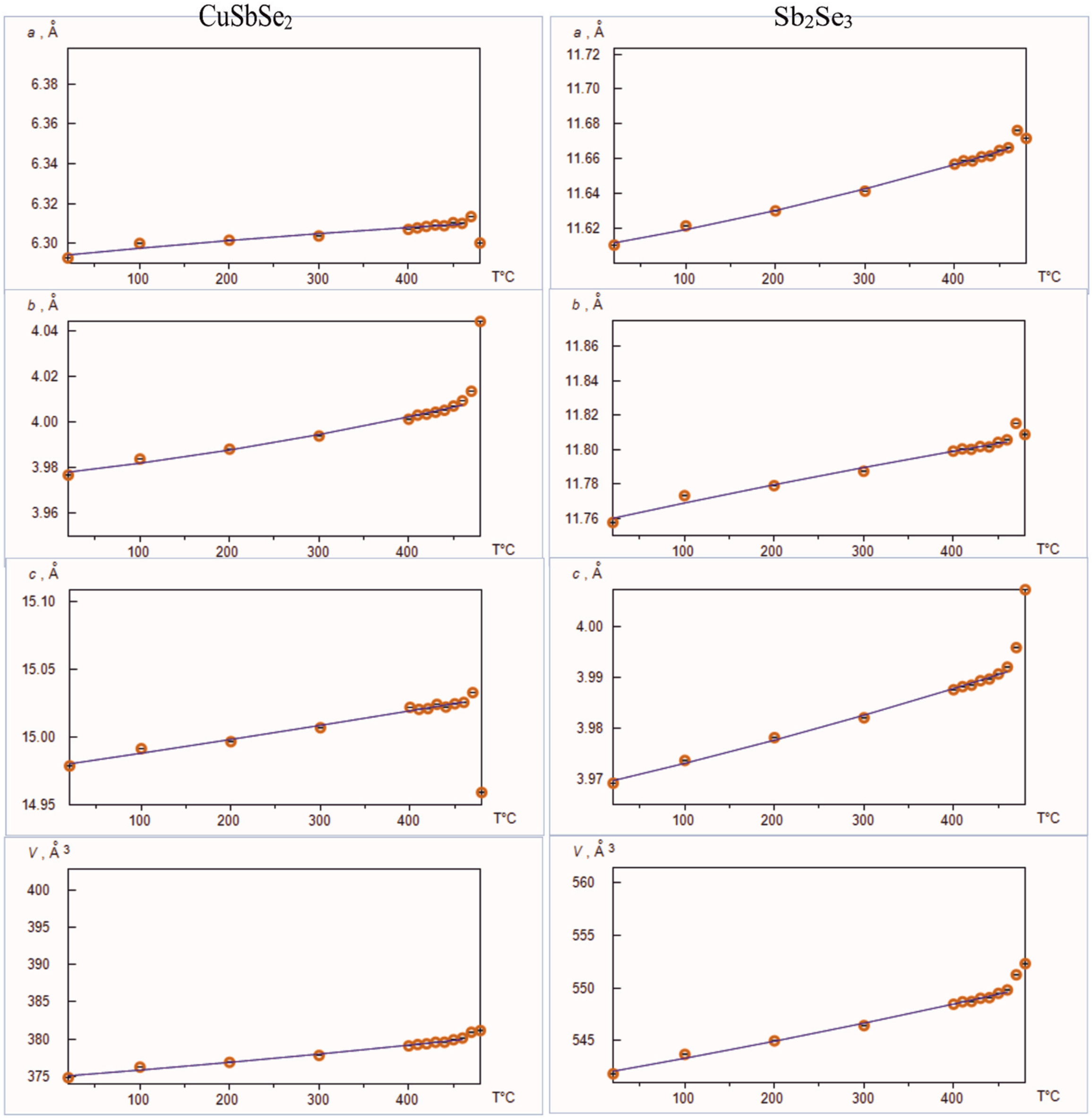

Fig. 10. Unit cell parameters of $CuSbSe_2$ and Sb_2Se_3 phases versus temperature in a 75 mol% Sb_2Se_3 + 25 mol% Cu_2Se sample.

the 20–460 °C temperature range (Table 4). Using the coefficients of approximation, the components of tensor (Table 5) were determined, and the drawing of the figures of α were performed using the Theta To Tensor & Rietveld to Tensor software [81,82].

Volume thermal expansion, α_V, gradually increases for both selenides within the temperature range under study; also, the anisotropy of thermal expansion defined as ratio $\alpha_{max}/\alpha_{min}$ rises for both phases when temperature increases (Table 5). Anisotropy for $CuSbSe_2$ is about 1.7 at 20 °C and it becomes about 5 at 450 °C, that for Sb_2Se_3 is about 1.4 at 20 °C and 1.9 at 450 °C. Volume expansion increase is caused by rising thermal vibrations.

The crystal structure of $CuSbSe_2$ expands dramatically within the area close to *b* direction and minimally within the area close to *a* direction (Table 5). The framework is formed by alternating layers of $CuSe_4$ tetrahedra and $SbSe_5$ square pyramids, the layers are arranged perpendicular to the *c* axis (Fig. 11). The covalent Sb—Se bonds in pyramids are stronger than the more ionic Cu—Se bond. The apical bond is the shortest (Sb–Se1 is 2.569 Å) in comparison with others

Table 4
Polynomial coefficients ($p_T = p_0 + p_1T + p_2T^2$) for approximation of the unit-cell parameters and V for $CuSbSe_2$ and Sb_2Se_3 within 20–460 °C.

Parameter	p_0	$p_1 \times 10^3$	$p_2 \times 10^6$	p_0	$p_1 \times 10^3$	$p_2 \times 10^6$
	$CuSbSe_2$			Sb_2Se_3		
a	6.2933(13)	0.044(13)	−0.019(25)	11.6100(13)	0.087(12)	0.076(23)
b	3.9773(13)	0.043(12)	0.050(24)	11.7578(21)	0.114(21)	-0.028(41)
c	14.9784(21)	0.097(20)	0.015(39)	3.96888(57)	0.0406(56)	0.017(10)
V	374.92(21)	9.1(2.1)	4.0(4.1)	541.78(22)	14.8(2.1)	4.7(4.1)

Table 5
Eigenvalues of thermal expansion tensor for $CuSbSe_2$ and Sb_2Se_3 phases at selected temperatures.

α (10^6 °C^{-1})	Temperature, *T*/ °C					
	20	100	200	300	400	450
$CuSbSe_2$						
$\alpha_a = \alpha_{11}$	7.1(2)	6.4(1.2)	5.8(6)	5.2(6)	4.6(1.2)	4.3(1.6)
$\alpha_b = \alpha_{22}$	10.8(3.1)	13.3(1.9)	15.8(9)	18.2(8)	20.7(1.8)	21.9(2.4)
$\alpha_c = \alpha_{33}$	6.5(1.3)	6.67(87)	6.9(4)	7.1(4)	7.24(82)	7.3(1)
α_V	24.4(5.6)	26.4(3.5)	28.5(1.6)	30.5(1.4)	32.5(3.3)	33.5(4.3)
$\alpha_{max}/\alpha_{min}$	1.66	2.1	2.72	3.5	4.5	5.09
Sb_2Se_3						
$\alpha_a = \alpha_{11}$	7.5(1)	8.8(7)	10.0(3)	11.3(3)	12.6(6)	13.3(8)
$\alpha_b = \alpha_{22}$	9.7(1.8)	9.2(1.1)	8.8(5)	8.3(5)	7.8(1)	7.5(1.4)
$\alpha_c = \alpha_{33}$	10.2(1.4)	11.1(9)	11.9(4)	12.7(4)	13.5(8)	14.0(1.1)
α_V	27.4(4)	29.1(2.5)	30.7(1.1)	32.3(1)	33.9(2.3)	34.7(3)
$\alpha_{max}/\alpha_{min}$	1.36	1.26	1.35	1.53	1.73	1.87

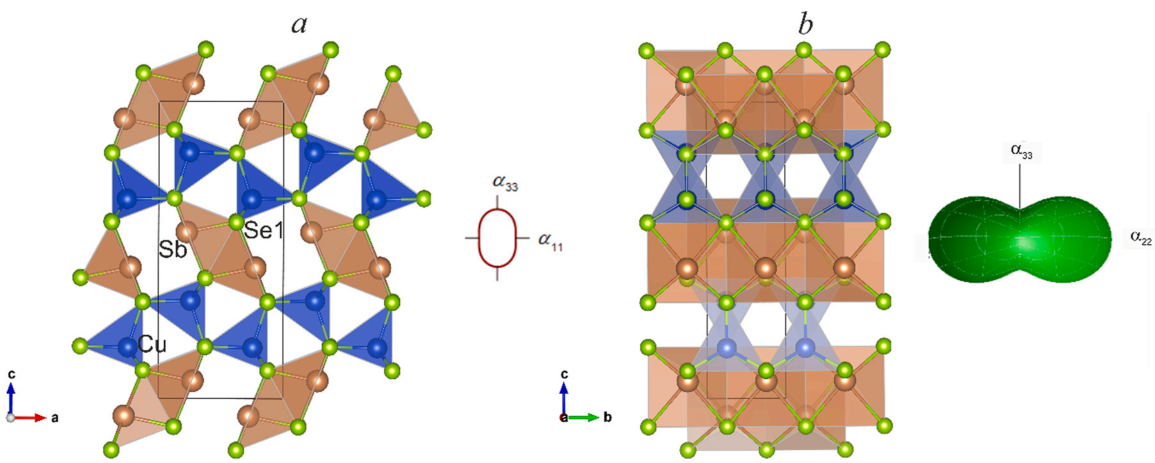

Fig. 11. The anisotropy of thermal expansion of $CuSbSe_2$ at 450 °C in the *ac* (*a*) and *cb* (*b*) planes in comparison to crystal structure.

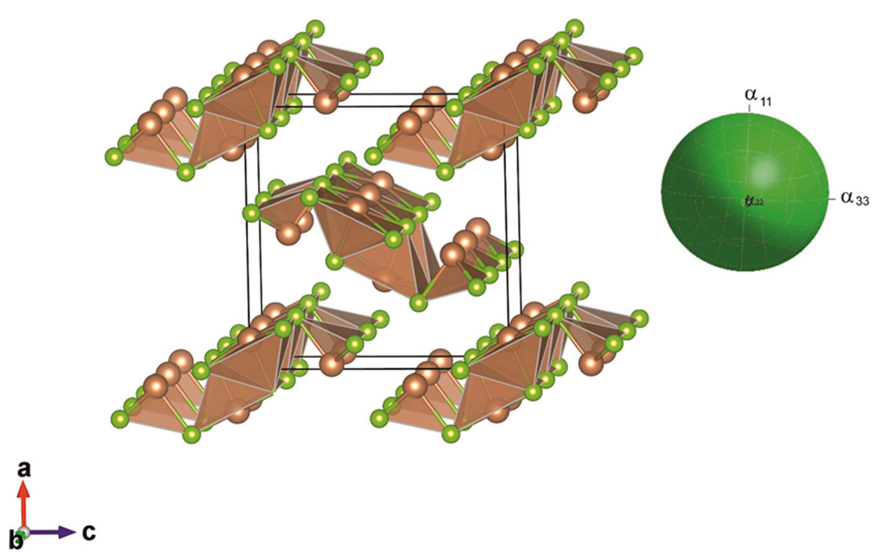

Fig. 12. General view of the Sb_2Se_3 crystal structure formed by the ribbons extending along the *b* axis (left) in comparison to thermal expansion tensor at 450 °C (right).

(2.702 Å and 3.202 Å) and therefore, this bond is the strongest. With an increase in temperature, the Cu–Se bonds in the $CuSe_4$ tetrahedra seem to elongate more than Sb–Se bonds in $SbSe_5$ pyramids, and the framework becomes distorted.

The thermal expansion is minimal in the *ac* plane especially along *a* axis due to the shortest and strongest Sb–Se1 bond (Fig. 11a) which is located about along this direction. The layers of $CuSe_4$ tetrahedra expand along the *b* axis direction and in this direction the thermal expansion is maximal (Fig. 11*b*).

Expansion between the layers is medium in the *c* direction. The nature of the strong anisotropy of thermal expansion up to negative within any area is described in detail in [103–106]. As a rule, a strong expansion along one direction causes a minimum up to a negative one in the perpendicular direction, and structure of $CuSbSe_2$

demonstrates similar anisotropy. The anisotropy of thermal expansion in the *ac* and *cb* planes at 450 °C in comparison to the crystal structure is shown in Fig. 11*a* and *b*, respectively. The anisotropy of thermal expansion of this selenide is similar to that of As_2S_3 (orpiment) [107].

The crystal structure of Sb_2Se_3 [31] consists of ribbons, containing two chains of $SbSe_5$ pyramids connected along the edges and chains of vertex-connected $SbSe_3$ distorted triangles in the projection on the *ac* plane (Fig. 12). The ribbons are elongated along the *b* axis (Fig. 12), and these ribbons are weakly bonded to each other. Therefore, with an increase in temperature, the expansion increases almost isotropically in the *ac* plane, while the expansion along the *b* axis slightly decreases because bonds along ribbons are very strong. It is notable that thermal expansion character of this selenide is similar to that of AsS realgar built up from isolated As_4S_4 molecules bonded by weak van der Waals interactions [107]. The average volume thermal expansion coefficient for both selenides ($<\alpha_V>_2$ = 30×10^{-6} °C^{-1}) is smaller than average volume thermal expansion coefficient for both sulfides ($<\alpha_V>_2$ = 108×10^{-6} °C^{-1}).

On heating, the anisotropy of thermal expansion (defined as ratio $\alpha_{max}/\alpha_{min}$ in Table 5) practically does not change for Sb_2Se_3 phase due to strong covalent bonds while it increases for $CuSbSe_2$ phase that may be caused by the presence of both covalent and ionic bonds.

The anisotropy of thermal expansion of the phase $CuSbSe_2$, distortion of the frame structure, and significant distortion of the $CuSe_4$ tetrahedra along the b axis determine the thermal instability of the $CuSbSe_2$ compound and increase its chemical activity. The interaction between the $CuSbSe_2$ and Sb_2Se_3 phases at 445 °C forms the ternary phase $CuSb_3Se_5$.

Three new diffraction peaks were recorded by HTXRD at temperatures of 470–480 °C. The values of *d* and 2θ for these peaks are shown in Fig. 9C. The main peaks of $CuSbSe_2$ and Sb_2Se_3 were also present on the diffraction pattern, but their unit cell parameters changed abruptly and in different directions (Fig. 10, isolated points). The diffraction patterns (Fig. 9) also contain several weak reflections with a lower intensity. Probably, weak peaks are caused by the appearance of impurity phases in the sample. Weak peaks could not be identified due to the small number and lack of information in diffractometric databases on suitable d values for phases from the Cu-Sb-Se-O system. The estimated content of these phases is no more than 0.5 mol%.

6. Properties of the $CuSb_3Se_5$ phase

An appreciable sublimation of the sample and an insufficient yield of the $CuSb_3Se_5$ did not allow us to obtain a complete X-ray diffraction pattern of this phase at 480 °C. Probably, in the $CuSb_3Se_5$ structure, the smaller number of $CuSe_4$ tetrahedra (the fourth part) prone to distortion determines the thermal stability of the phase.

The high-temperature phase $CuSb_3Se_5$ is stable over time. A sample containing 75 mol% Sb_2Se_3 was annealed at t = 480 ± 10 °C during 4300 h in an evacuated and sealed quartz ampoule, which was at an angle to the horizontal line during annealing. Annealing resulted in the formation of a compact solid sample. If the $CuSb_3Se_5$ phase would decompose during annealing, then the Sb_2Se_3 crystalline phase and liquid should have been formed. In this case, the sample would have to spread over the ampoule. The sample did not separate into its component parts and remained compact during annealing. After cooling, the sample had the following phase composition: 47 mol% Sb_2Se_3, 41 mol% $CuSbSe_2$, 12 mol% Cu_3SbSe_3. The grain structure of the sample after cooling was similar to the grain structure of the sample after DSC (Fig. 8E).

Thus, HTXRD and annealing results for a sample containing 75 mol% Sb_2Se_3 at 480 ± 10 °C confirm the formation of the high-temperature phase $CuSb_3Se_5$.

The $CuSbSe_2$ and $CuSb_3Se_5$ phases do not form eutectic mixtures. The DSC curves for the samples containing from 50 to 71 mol% Sb_2Se_3 feature the following thermal events: $CuSb_3Se_5$ formation at 445 °C, incongruent melting of $CuSbSe_2$ at 478 °C, and melting of the crystals produced during incongruent melting of $CuSbSe_2$ (Fig. 5: sample (5)). The DSC curves contain exotherms of the following phase transformations: formation of $CuSb_3Se_5$ primary crystals at 480 °C, $CuSbSe_2$ formation at 430 °C, and superposition of peaks due to $CuSb_3Se_5$ decomposition and eutectic (1 Cu_3SbSe_3 + 8 $CuSbSe_2$) solidification at 424 °C. The liquidus temperature systematically and monotonically increases in the concentration range 50–71 mol% Sb_2Se_3.

7. Peculiarities of phase equilibria in the $Cu_{2-X}Se$-Sb_2Se_3 system in the concentration range 0–25 mol% Sb_2Se_3

The 2.00Cu:1.00Se-Sb_2Se_3 section in the concentration range 0–25 mol% Sb_2Se_3 crosses several subordinate systems of the Cu-Sb-Se triangle. In the sample containing 0.5 mol% Sb_2Se_3 (Fig. 13a) the $Cu_{2-X}Se$ and Sb phases are present. Antimony Sb grains are located in the form of strips between the $Cu_{2-X}Se$ grains. With an increase in the content of Sb_2Se_3, the samples become three-phase. The $Cu_{2-X}Se$ phase binds an increased content of selenium, which is thus included in its composition. Selenium content is not sufficient to form the Cu_3SbSe_3 phase with stoichiometric composition. The elementary substance Sb is concentrated in the form of grains inside the Cu_3SbSe_3 phase (Fig. 13b). Samples from the 1.990Cu:1.000Se - Cu_3SbSe_3 and 1.970Cu:1.000Se - Cu_3SbSe_3 sections contain single antimony grains (Fig. 13c). Only in the 1.930Cu:1.000Se - Cu_3SbSe_3 section the presence of antimony as an elementary substance was not detected (Fig. 13d).

The presence of both low-temperature and high-temperature modifications of the $Cu_{2-X}Se$ phase is observable on the diffraction patterns of the cooled samples, which confirms the formation of the $Cu_{2-X}Se$-based solid solution in the Cu-Sb-Se system (Fig. 7). The Cu_3SbSe_3 phase is most likely in equilibrium with a $Cu_{2-X}Se$-based solid solution of variable composition for X values: $1.97 \pm 0.01 < X \le 1.93 \pm 0.01$. The content of copper and selenium in the $Cu_{2-X}Se$ phase in each of the samples was determined by the SEM method for five to seven points on the sample surface. Average values are shown in Table 6. For two samples, the X values in the $Cu_{2-X}Se$ phase composition were obtained, which are included in the mentioned above interval (Table 6).

The $Cu_{2-X}Se$-Sb_2Se_3 system phase diagram represents data for samples from 1.99Cu:1.00Se-Cu_3SbSe_3 section for two reasons.

Sample with stoichiometry 1.99Cu:1.00Se in the $Cu_{2-X}Se$-based solid solution area has a maximum melting point 1145 °C. The DSC-curves of samples from this section show a slight decrease (up to 5 °C) in the temperature of incongruent melting of the Cu_3SbSe_3 phase.

For samples from the 1.950Cu:1.000Se-Cu_3SbSe_3 and 1.930Cu:1.000Se-Cu_3SbSe_3 sections the peak of Cu_3SbSe_3 phase incongruent melting becomes blurred, its temperature drops by 10–20 °C.

8. Thermodynamic modeling using the Redlich-Kister polynomial

The liquidus consists of five segments. In each of the four segments, from 8 to 11 data points were obtained, and these segments were approximated by second-order or third-order polynomials. Since the eutectic lies in the area of more high concentrations of the refractory component, it was necessary to compare the results of thermal studies with the results of calculations.

From the Redlich-Kister polynomial for subsequent calculations of the liquidus line position, the expressions for the activity coefficients and chemical potentials of the components in the melt

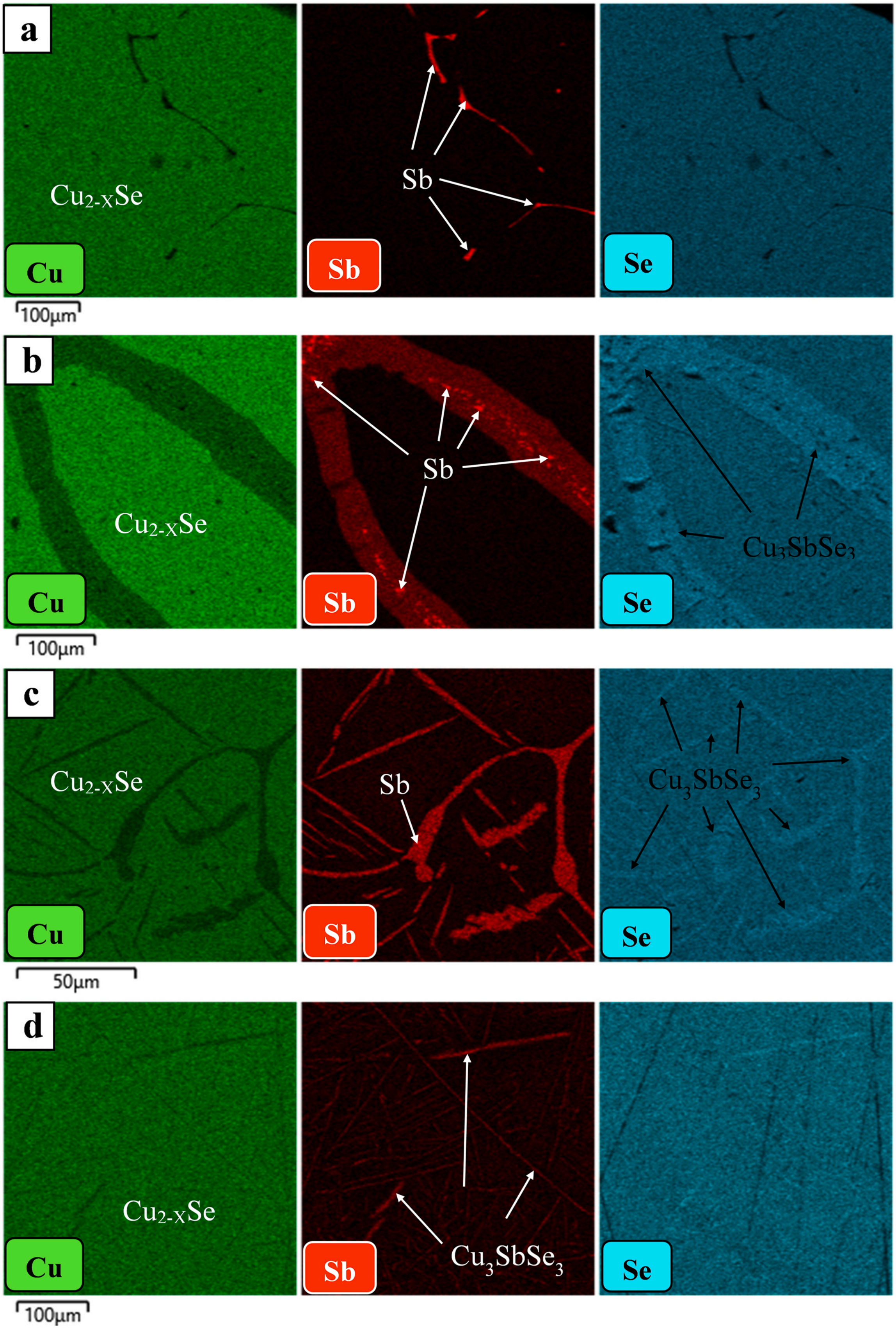

Fig. 13. SEM images illustrating the Cu, Sb, and Se concentrations in polished thin sections of annealed samples. Notations: as-batch (global) composition – phase composition. a – 99.5 mol% 2.00Cu:1.00Se 0.5 mol% Sb_2Se_3 – $Cu_{2-x}Se$, Sb; b – 95.0 mol% 2.00Cu:1.00Se 5.0 mol% Cu_3SbSe_3 – $Cu_{2-x}Se$, Cu_3SbSe_3, Sb; c – 95.0 mol% 1.97Cu:1.00Se 5.0 mol% Cu_3SbSe_3 – $Cu_{2-x}Se$, Cu_3SbSe_3, Sb (single grains); d - 95.0 mol% 1.93Cu:1.00Se 5.0 mol% Cu_3SbSe_3 – $Cu_{2-x}Se$, Cu_3SbSe_3.

Table 6
Mass percentage of Cu and Se in the $Cu_{2-x}Se$ phase according to weighted portion calculation data and SEM data.

	2.00 Cu: 1.00 Se	1.97 Cu: 1.00 Se	1.93 Cu: 1.00 Se
	Weighted portion calculation data		
Cu	61.56%	61.32%	60.83%
Se	38.44%	38.68%	39.17%
	SEM data		
Cu	61.3	60.3%	60.7%
Se	38.7	39.7%	39.3%
$Cu_{2-x}Se$ phase composition according to SEM data	$Cu_{1.97}Se$	$Cu_{1.89}Se$	$Cu_{1.92}Se$

(solution) were obtained. This liquidus calculation model was successfully used to plot phase diagrams for similar systems [108–110].

The Redlich-Kister polynomial describes the variation of the excess Gibbs free energy and the activity coefficients of the components depending on the composition and temperature in the system. Molar excess Gibbs energy for a binary solution is expressed by the following Eq. (1):

$$\Delta G = x_1x_2\left[L_0 + L_1\left(x_1 - x_2\right) + L_2(x_1 - x_2)^2 + .\right] = x_1x_2\sum_{j=0}^{k} L_j(x_1 - x_2)^j \quad (1)$$

where x_1 and x_2 the are molar fractions of components in the melt and L_j are numerical factors (the interaction parameters).

The temperature effect on the excess thermodynamic functions of the liquid is taken into account in the equation for the excess Gibbs energy $RT\ \ln\gamma\ = \Delta G_m^E$ and is expressed by the equations for activity coefficients of the components while retaining the first three terms. The equations for activity coefficients of the binary solution components were obtained [70] (2), (3):

$$RT\ \ln\gamma_1 = (1 - x_1)^2\left[L_0 + L_1\left(4x_1 - 1\right) + L_2\left(12x_1^2 - 8x_1 + 1\right)\right] \quad (2)$$

$$RT\ \ln\gamma_2 = x_1^2\left[L_0 + L_1\left(4x_1 - 3\right) + L_2\left(12x_1^2 - 16x_1 + 5\right)\right] \quad (3)$$

where γ_1 and γ_2 are activity coefficients of the 1st and 2nd component, respectively; and L_0, L_1, and L_2 are numerical factors.

This is enough to write down expressions for chemical potentials and subsequently calculate the liquidus line of the system.

The chemical potentials of components may be expressed by the following equations:

$$\mu_1 = \mu_1^0 + RT\ \ln x_1 + (1 - x_1)^2\left[L_0 + L_1\left(4x_1 - 1\right) + L_2\left(12x_1^2 - 8x_1 + 1\right)\right] \quad (4)$$

$$\mu_2 = \mu_2^0 + RT\ \ln x_2 + x_1^2\left[L_0 + L_1\left(4x_1 - 3\right) + L_2\left(12x_1^2 - 16x_1 + 5\right)\right] \quad (4)$$

where μ_1^0, μ_2^0 are standard chemical potentials of component 1 and component 2, respectively. Subscript “1” refers to Cu_2Se, and subscript “2” refers to Sb_2Se_3.

The temperature effect on the coefficients L for the melt is taken into account. The coefficients are found for a specific equilibrium temperature taken from the experimental data, thus taking into account its effect.

The entropy contribution to the stability of solid phases, of course, is present. But since the solid phases are stable and are being in equilibrium with the melt, this contribution for the equilibrium “solid component-melt” was not determined separately. The activity of the pure solid component is 1. The melting entropy contribution to the equilibrium is partially taken into account in Eq. (6) and subsequent transformations.

$$-RT\ \ln a_i = \frac{\Delta H_{m.i}(T_{m.i} - T)}{T_{m.i}}, \quad (6)$$

where a_i is activity of the i^{th} component in the melt, $\Delta H_{m.i}$ is enthalpy of melting of the pure ith component, $T_{m.i}$ is melting temperature of the i^{th} component, and T is temperature of the equilibrium melt. Then, taking into account the generally accepted formula:

$$\mu = \mu^0 + RT\ \ln a, \quad (7)$$

for the first component we have

$$RT\ \ln a_1 = RT\ \ln x_1 + (1 - x_1)^2\left[L_0 + L_1\left(4x_1 - 1\right) + L_2\left(12x_1^2 - 8x_1 + 1\right)\right] \quad (8)$$

and the expression for equilibrium becomes

$$\frac{\Delta H_{m.1}(T_{m.1} - T)}{T_{m.1}} = -\left[RT\ \ln x_1 + (1 - x_1)^2\left[L_0 + L_1\left(4x_1 - 1\right) + L_2\left(12x_1^2 - 8x_1 + 1\right)\right]\right] \quad (9)$$

For example, the calculation equation for the equilibrium "melt - component Sb_2Se_3" at a temperature of 529 °C will look like:

$$\frac{\Delta H_{m.2}(T_{m.2} - T)}{T_{m.2}} = -\left[RT\ \ln x_2 + x_1^2\left[L_0 + L_1\left(4x_1 - 3\right) + L_2\left(12x_1^2 - 16x_1 + 5\right)\right]\right] \quad (10)$$

where $\Delta H_{m.2}$ is the enthalpy of melting of the Sb_2Se_3 component, and x_2 = 0.71 and x_1 = 0.29 are, respectively, Sb_2Se_3 and Cu_2Se mole fractions at the equilibrium temperature T = 527 °C (800 K). Similar equations for phase equilibria in the other invariant points can be written (Table 3, Eqs. (1)–(5)) [108].

The melting enthalpies for the components of the system were obtained by DSC. The approaches described in the paper [111], where the thermal characteristics of complex chalcogenides were determined, were used. The temperature and enthalpy of melting for Sb_2Se_3 were found to be: T_m = 612 °C and ΔH_m = 50.2 ± 5.8 KJ/mol. These values nearly coincided with previously reported values: T_m = 611 °C [36], and ΔH_m = 50.2 ± 4.2 kJ/mol [37].

Samples of the copper semiselenide $Cu_{2-x}Se$ based solid solution area were synthesized with the next ratios for elementary substances placed in ampoules: 2.000 Cu: 1.000 Se (1), 1.990 Cu: 1.000 Se (2), 1.970 Cu: 1.000 Se (3), 1.930 Cu: 1.000 Se (4). For samples (1) and (2), the melting peaks have a pronounced linear section, indicating the transition of the sample into a melt at a constant temperature. The rest of the samples melted within a certain temperature range. The melting enthalpies and melting temperatures, respectively, are: $\Delta H_m(1)$ = 9.7 ± 1.1 kJ/mol, $T_m(1)$ = 1143 °C; $\Delta H_m(2)$ = 8.7 ± 1.0 kJ/mol, $T_m(2)$ = 1145 °C; $\Delta H_m(3)$ = 5.2 ± 1.0 kJ/mol, $T_m(3)$ = 1108–1135 °C; $\Delta H_m(4)$ = 4.7 ± 1.0 kJ/mol, $T_m(4)$= 1087–1132 °C.

The values determined for the enthalpies of melting agree, within the determination error, with the values reported for Cu_2Se T_m= 1117 °C, and ΔH_m= 9.055 kJ/mol [25]. To calculate the liquidus line according to the obtained equations, we used the data for the sample (2).

The solution of the equations system gave the following numerical values: L_0 = –15,390, L_1 = 24,400, and L_2 = – 27,740. The liquidus line was calculated for each range as a temperature versus composition function. The calculated liquidus is shown by the dashed line in Fig. 5.

The discrepancy between the liquidus curve plotted by fitting DSC data and the curve calculated by the Redlich-Kister method is 1–13 °C in the range 0–32 mol% Sb_2Se_3, 1–7 °C in the range 32–45 mol% Sb_2Se_3, and 1–3 °C in the range 71–100 mol% Sb_2Se_3. The largest discrepancy (1–17 °C) was observed in the range 46–71 mol% Sb_2Se_3. The calculated liquidus is a convex curve, that is the most frequent type of liquidus. The experimental liquidus shows an insignificant concavity. The trend of the liquidus in that range correlates with the existence of the unstable high-temperature phase $CuSb_3Se_5$, whose primary crystals are formed upon cooling precisely in the range 46–71 mol% Sb_2Se_3. In general, the results of the calculation of the liquidus line using the Redlich-Kister polynomial obtained from the data for phase equilibria at invariant points of the $Cu_{2-X}Se$-Sb_2Se_3 system agrees with the DSC data, supporting the correctness of the phase diagram.

Comparison of the obtained the $Cu_{2-X}Se$-Sb_2Se_3 system phase diagram with literature data (Figs. 2 and 5).

In the present work, like in [39] and [40], the existence of the $CuSbSe_2$ compound, which forms a eutectic towards the $Cu_{2-X}Se$ component, is confirmed. Like the author of [19], we confirmed the existence of three ternary compounds in the system, including the high-temperature phase $CuSb_3Se_5$. In this paper, for the first time, the thermal characteristics of phases, a number of their properties, and the position of phase equilibrium lines in $Cu_{2-X}Se$-Sb_2Se_3 systems are presented.

9. Conclusions

The re-determination of the phase diagram in this system combined with a careful characterization of all the phases in the system by a complex of instrumental techniques helped to resolve the discrepancy in the earlier published results [19,30,39,40,47].

We have confirmed unambiguously that the three ternary compounds –Cu_3SbSe_3, $CuSbSe_2$, $CuSb_3Se_5$ – can exist in the $Cu_{2-X}Se$-Sb_2Se_3 system. The formation of $CuSb_3Se_5$ was proved by high-temperature X-ray diffraction of a sample containing 75 mol% Sb_2Se_3 and 25 mol% Cu_2Se. During the experiment the sample sublimed, and the completeness of the reaction was not high enough, therefore the diffraction data from the small amount of the $CuSb_3Se_5$ phase were not sufficient to solve its structure. A high-temperature X-ray diffraction study of the sample containing 75 mol% Sb_2Se_3 and 25 mol% Cu_2Se allowed us to follow the anisotropy of thermal expansion of the $CuSbSe_2$ and Sb_2Se_3 phases. Volume thermal expansion, α_V, gradually increases for both selenides within the range under study. For both selenides the increase in volume expansion is caused by rising thermal atomic vibrations. The anisotropy of thermal expansion of $CuSbSe_2$ and Sb_2Se_3 was similar to those of the well-studied As sulfides, As_2S_3 and AsS, respectively.

The up-dated phase diagram obtained in our work now takes into consideration the existence of all the three compounds (Cu_3SbSe_3, $CuSbSe_2$ and $CuSb_3Se_5$) and their participation in the phase equilibria. The phase identities were proven by a complex of methods including structure solution and refinement by single-crystal X-ray diffraction, powder X-ray diffraction, measurements of the energy bandgaps. The exact range of the existence of $Cu_{10.53}Sb_{33.78}Se_{55.68}$ was found from the DSC and high-temperature X-ray diffraction; previously it was only roughly estimated [19]. Six balance equations of the invariant phase transformations were suggested, that take into account the participation of all the three ternary compounds in the $Cu_{2-x}Se$-Sb_2Se_3 system. In the system, the Cu_3SbSe_3 phase is in equilibrium with the $Cu_{2-X}Se$ solid solution of non-stoichiometric composition. The temperatures and the enthalpies of these invariant transformations were determined. The liquidus curve is calculated for this system using Redlich-Kister polynomial coincided within 1–17 °C with the DSC data. The consistence of the results obtained by many independent methods allow us to consider that new phase diagram obtained in the present work as reliable.

CRediT authorship contribution statement

M.A. Shtykova: Data curation, Visualization, Supervision, Project administration, Writing – original draft. **M.S. Molokeev:** Formal analysis. **B.A. Zakharov:** Investigation, Resources, Methodology, Formal analysis, Visualization, Data curation, Funding acquisition. **N.V. Selezneva:** Investigation, Formal analysis, Resources. **A.S. Aleksandrovsky:** Formal analysis, Writing – review & editing, Validation. **R.S. Bubnova:** Software, Formal analysis, Visualization, Funding acquisition. **D.N. Kamaev:** Formal analysis, Visualization. **A.A. Gubin:** Investigation, Resources. **N.N. Habibullaev:** Investigation, Visualization, Data curation. **A.V. Matigorov:** Resources, Investigation. **E.V. Boldyreva:** Supervision, Writing – review & editing, Validation, Data curation. **O.V. Andreev:** Conceptualization, Methodology, Software, Validation, Resources, Data curation, Writing – original draft, Project administration, Funding acquisition, Supervision.

Declaration of Competing Interest

The authors declare that they have no known competing financial interests or personal relationships that could have appeared to influence the work reported in this paper.

Acknowledgments

The research was supported for R.S. Bubnova by the Ministry of Science and Higher Education of the Russian Federation within the scientific tasks of the Institute of Silicate chemistry (Russian Academy of Sciences) [project number 0097-2019-0013].

The equipment of Research and Education Center "Molecular design and ecologically safe technologies" (Novosibirsk State University) was used for single-crystal X-ray diffraction experiments. BAZ and EVB acknowledge support by the Ministry of Science and Higher Education, project AAAA-A21-121011390011-4.

Appendix A. Supplementary material

Supplementary data associated with this article can be found in the online version at doi:10.1016/j.jallcom.2022.164384.

References

[1] R.J. Mehta, C. Karthik, W. Jiang, B. Singh, Y. Shi, W. Richard, T. Siegel, G. Borca-Tasciuc, Ramanath, High electrical conductivity antimony selenide nanocrystals and assemblies, Nano Lett. 10 (2010) 4417–4422, https://doi.org/10.1021/nl1020848

[2] H. Liu, X. Shi, F. Xu, L. Zhang, W. Zhang, L. Chen, Q. Li, C. Uher, T. Day, G.J. Snyder, Copper ion liquid-like thermoelectrics, Nat. Mater. 11 (2012) 422–425, https://doi.org/10.1038/nmat3273

[3] Y. Zhang, X. Shao, Y. Zheng, L. Yan, P. Zhu, Y. Li, H. Xu, Pressure-induced structural transitions and electronic topological transition of Cu_2Se, J. Alloy. Compd. 732 (2018) 280–285, https://doi.org/10.1016/j.jallcom.2017.10.201

[4] J.J. Carey, J.P. Allen, D.O. Scanlon, G.W. Watson, The electronic structure of the antimony chalcogenide series: prospects for optoelectronic applications, J. Solid State Chem. 213 (2014) 116–125, https://doi.org/10.1016/j.jssc.2014.02.014

[5] A.U. Ubale, D.M. Choudhari, J.S. Kantale, V.N. Mitkari, M.S. Nikam, W.J. Gawande, P.P. Patil, Synthesis of nanostructured Cu_xS thin films by chemical route at room temperature and investigation of their size dependent physical properties, J. Alloy. Compd. 509 (2011) 9249–9254, https://doi.org/10.1016/j.jallcom.2011.07.009

[6] V.A. Kulbachinskii, A.A. Kudryashov, V.G. Kytin, The Shubnikov-de Haas effect and thermoelectric properties of Tl-doped Sb_2Te_3 and Bi_2Se_3, Semiconductors 49 (2015) 767–773, https://doi.org/10.1134/S1063782615060135

[7] H. Kim, M.-K. Han, C.-H. Yo, W. Lee, S.-J. Kim, Effects of Bi_2Se_3 nanoparticle inclusions on the microstructure and thermoelectric properties of Bi_2Te_3-based nanocomposites, J. Electron. Mater. 41 (2012) 3411–3416, https://doi.org/10.1007/s11664-012-2255-7

[8] A. Yamamoto, K. Ogawa, T. Takeuchi, Effect of chemical potential on thermoelectric power of Bi_2Te_3 and Bi_2Se_3, Mater. Trans. 52 (2011) 1539–1545, https://doi.org/10.2320/matertrans.E-M2011809

[9] X. Yan, B. Poudel, Y. Ma, W.S. Liu, G. Joshi, H. Wang, Y. Lan, D. Wang, G. Chen, Z.F. Ren, Experimental studies on anisotropic thermoelectric properties and structures of n-type $Bi_2Te_{2.7}Se_{0.3}$, Nano Lett. 10 (2010) 3373–3378, https://doi.org/10.1021/nl101156v

[10] A. Singh, P. Shahi, A.K. Ghosh, J.G. Cheng, S. Chatterjee, Enhancement in power factor due to anti-correlation between electrical conductivity and thermoelectric power and induced magnetic ordering in high mobility Zn doped Bi_2Te_3 topological insulator, J. Alloy. Compd. 731 (2018) 297–302, https://doi.org/10.1016/j.jallcom.2017.10.039

[11] Z.-L. Wang, T. Akao, T. Onda, Z.-C. Chen, Microstructure and thermoelectric properties of Bi-Sb-Te bulk materials fabricated from rapidly solidified powders, Scr. Mater. 136 (2017) 111–114, https://doi.org/10.1016/j.scriptamat.2017.04.032
[12] B.R. Chakraborty, B. Ray, R. Bhattacharya, A.K. Dutta, Magnetic and electric properties of antimony selenide (Sb_2Se_3) crystals, J. Phys. Chem. Solids 41 (1980) 913–917, https://doi.org/10.1016/0022-3697(80)90037-2
[13] T.-R. Wei, C.-F. Wu, F. Li, J.-F. Li, Low-cost and environmentally benign selenides as promising thermoelectric materials, J. Mater. 4 (2018) 304–320, https://doi.org/10.1016/j.jmat.2018.07.001
[14] C. Gayner, Y. Amouyal, Energy filtering of charge carriers: current trends, challenges, and prospects for thermoelectric materials, Adv. Funct. Mater. (2019) 1901789, https://doi.org/10.1002/adfm.201901789
[15] C. Gayner, K.K. Kar, Recent advances in thermoelectric materials, Prog. Mater. Sci. 83 (2016) 330–382, https://doi.org/10.1016/j.pmatsci.2016.07.002
[16] H. Zhu, J. Mao, Z. Feng, J. Sun, Q. Zhu, Z. Liu, D.J. Singh, Y. Wang, Z. Ren, Understanding the asymmetrical thermoelectric performance for discovering promising thermoelectric materials, Sci. Adv. 5 (2019), https://doi.org/10.1126/sciadv.aav5813 eaav5813.
[17] X. Shi, L. Chen, C. Uher, Recent advances in high performance bulk thermoelectric materials, Int. Mater. Rev. 61 (6) (2016) 379–415, https://doi.org/10.1080/09506608.2016.1183075
[18] D. Beretta, N. Neophytou, J.M. Hodges, M.G. Kanatzidis, D. Narducci, M. Martin-Gonzalez, M. Beekman, B. Balke, G. Cerretti, W. Tremel, A. Zevalkink, A.I. Hofmann, C. Müller, B. Dörling, M. Campoy-Quiles, M. Caironi, Thermoelectrics: from history, a window to the future, Mater. Sci. Eng. R Rep. 138 (2019) 210–255, https://doi.org/10.1016/j.mser.2018.09.001
[19] S. Karup-Moller, The Cu-Sb-Se phase system at temperatures between 350° and 700°C, Neues Jahrb. Miner. Abh. 174 (1999) 277–292, https://doi.org/10.1127/njma/174/1999/277
[20] S. Fürtauer, H. Flandorfer, A new experimental phase diagram investigation of Cu-Sb, Mon. Chem. 143 (2012) 1275–1287, https://doi.org/10.1007/s00706-012-0737-1
[21] G. Ghosh, The Sb-Se (antimony-selenium) system, J. Phase Equilib. 14 (1993) 753–763, https://doi.org/10.1007/BF02667889
[22] V.M. Glazov, A.S. Pashinkin, V.A. Fedorov, Phase equilibria in the Cu-Se system, Inorg. Mater. 36 (2000) 641–652, https://doi.org/10.1007/BF02758413
[23] H. Kim, S. Ballikaya, H. Chi, J.-P. Ahn, K. Ahn, C. Uherc, M. Kavianya, Ultralow thermal conductivity of β-Cu_2Se by atomic fluidity and structure distortion, Acta Mater. 86 (2015) 247–253, https://doi.org/10.1016/j.actamat.2014.12.008
[24] J.O. Thompson, M.D. Anderson, T. Ngai, T. Allen, D.C. Johnson, Nucleation and growth kinetics of co-deposited copper and selenium precursors to form metastable copper selenides, J. Alloy. Compd. 509 (2011) 9631–9637, https://doi.org/10.1016/j.jallcom.2011.07.042
[25] R.M. Murray, R.D. Heyding, The copper-selenium system at temperatures to 850 K and pressures to 50 kbar, Can. J. Chem. 53 (1975) 878–887, https://doi.org/10.1139/v75-122
[26] L.D. Gulay, M. Daszkiewicz, O.M. Strok, A. Pietraszko, Crystal structure of Cu_2Se, Chem. Met. Alloy. 4 (2011) 200–205, https://doi.org/10.30970/cma4.0184
[27] E. Eikeland, A.B. Blichfeld, K.A. Borup, K. Zhao, J. Overgaard, X. Shi, L. Chen, B.B. Iversen, Crystal structure across the b to a phase transition in thermoelectric $Cu_{2-x}Se$, IUCrJ 4 (2017) 476–485, https://doi.org/10.1107/S2052252517005553
[28] B. Gather, R. Blachnik, Temperature-composition diagrams in the Cu_2(Vib)-(Vb) sections of the ternary Cu-(Vb)-(Vib) systems (Vb = As, Sb, Bi; Vib = S, Se, Te), J. Less Common Met. 48 (1976) 205–212, https://doi.org/10.1016/0022-5088(76)90003-5
[29] R. Blachnik, P.-G. Gunia, Enthalpien von kupfer- und silberchalkogeniden, Z. Nat. 33a (1978) 190–196, https://doi.org/10.1515/zna-1978-0214
[30] M.A. Korzhuev, V.F. Bankina, B.F. Gruzinov, G.S. Bushmarina, Elektrofizicheskie svoystva superionnogo $Cu_{2-x}Se$ (the electrophysical properties of superionic $Cu_{2-x}Se$), Semiconductors 23 (1989) 1545–1551 ⟨http://journals.ioffe.ru/articles/29905⟩(accessed 18 January 2022).
[31] R. Caracas, X. Gonze, First-principles study of the electronic properties of A_2B_3 minerals, with A=Bi, Sb and B=S, Se, Phys. Chem. Miner. 32 (2005) 295–300, https://doi.org/10.1007/s00269-005-0470-y
[32] G.P. Voutsas, A.G. Papazoglou, P.J. Rentzeperis, The crystal structure of antimony selenide, Sb_2Se_3, Z. Krist. Cryst. Mater. 171 (1985) 261–268, https://doi.org/10.1524/zkri.1985.171.14.261
[33] M. Min, J. Zhai, X. Wang, B. Shen, G. Wen, T. Fan, Refinement of the crystal structure for a new mineral - antimonselite, Chin. Sci. Bull. 43 (1998) 413–416, https://doi.org/10.1007/BF02883722
[34] N.W. Tideswell, F.H. Kruse, J.D. McCullough, The crystal structure of antimony selenide, Sb_2Se_3, Acta Crystallogr. 10 (1957) 99–102, https://doi.org/10.1107/S0365110×57000298
[35] Antimony Selenide, Sb2Se3 (orthorhombic)" C 13.44, Standard X-ray Diffraction Powder Patterns, Section 3, Data for 51 Substances, National Bureau of Standards (U. S.)/U.S. Department of Commerce, Issued July 31, 1964, p. 7. ⟨https://digital.library.unt.edu/ark:/67531/metadc13211/⟩. (Accessed 18 January 2022).
[36] K.A. Chandrasekharan, A.G. Kunjomana, Growth and microindentation analysis of pure and doped Sb_2Se_3 crystals, Turk. J. Phys. 33 (2009) 209–217, https://doi.org/10.3906/fiz-0812-8
[37] R. Blachnik, A. Schneider, Schmelzwarmen von III/V-, IV/V- und V/VI-Verbindungen, Z. Anorg. Allg. Chem. 372 (1970) 314–324, https://doi.org/10.1002/zaac.19703720308
[38] R. Blachnik, A. Schneider, High-temperature enthalpies of As_2Te_3, Sb_2Se_3, Bi_2Se_3, GeAs, $GeAs_2$, and SnAs, J. Chem. Thermodyn. 3 (1971) 227–233, https://doi.org/10.1016/S0021-9614(71)80107-6
[39] V.M. Glazov, A.N. Krestovnikov, R.A. Kuliev, Issledovanie fazovogo ravnovesiya i analiz haraktera mezhmolekulyarnogo vzaimodejstviya v sistemah, obrazovannyh hal'kogenidami medi i sur'my (investigation of phase equilibrium and analysis of the nature of intermolecular interaction in systems formed by copper and antimony chalcogenides), Zhurnal Fiz. Khimii Russ. J. Phys. Chem. 43 (1969) 3063–3066.
[40] M.I. Golovei, V.I. Tkachenko, M.Y. Rigan, N.P. Stasyuk, Diagramma sostoyanija sistemy Cu_2Se-Sb_2Se_3 v oblasti soedinenija $CuSbSe_2$ (phase-diagram of the system Cu_2Se–Sb_2Se_3 in the region of the existence of the compound $CuSbSe_2$), Neorg. Mater. Inorg. Mater. 26 (1990) 786–788 https://scholar.google.com/scholar?hl=ru&as_sdt=0%2C5&q=Phase-diagram+of+the+system+Cu2Se–Sb2Se3+in+the+region+of+the+existence+of+the+compound+CuSbSe2&btnG= (accessed 18 January 2022).
[41] R.M. Imamov, Z.G. Pinsker, A.I. Ivchenko, Opredelenie kristallicheskoj struktury $CuSbSe_2$ (determination of the crystal structure of $CuSbSe_2$), Krist. Sov. Phys. Crystallogr. 9 (1964) 721–724 ⟨https://scholar.google.com/scholar?hl=ru&as_sdt=0%2C5&q=R.M.+Imamov%2C+Z.G.+Pinsker%2C+A.I.+Ivchenko%2C+Determination+of+crystal+structure+of+CuSbSe&btnG=⟩ accessed 18 January 2022.
[42] J. Zhou, G.-Q. Bian, Q.-Y. Zhu, Y. Zhang, C.-Y. Li, J. Dai, Solvothermal crystal growth of $CuSbQ_2$ (Q=S, Se) and the correlation between macroscopic morphology and microscopic structure, J. Solid State Chem. 182 (2009) 259–264, https://doi.org/10.1016/j.jssc.2008.10.025
[43] K. Ramasamy, R.K. Gupta, S. Palchoudhury, S. Ivanov, A. Gupta, Layer-structured copper antimony chalcogenides ($CuSbSe_xS_{2-x}$): stable electrode materials for supercapacitors, Chem. Mater. 27 (2015) 379–386, https://doi.org/10.1021/cm5041166
[44] J. Baker, R.S. Kumar, D. Sneed, A. Connolly, Y. Zhang, N. Velisavljevic, J. Paladugu, M. Pravica, C. Chen, A. Cornelius, Y. Zhao, Pressure induced structural transitions in $CuSbS_2$ and $CuSbSe_2$ thermoelectric compounds, J. Alloy. Compd. 643 (2015) 186–194, https://doi.org/10.1016/j.jallcom.2015.04.138
[45] P. Škácha, J. Sejkora, J. Plášil, Bytízite, IMA 2016-044. CNMNC Newsletter No. 33, October 2016, p. 1138, Mineral. Mag., 80, 2016, pp. 1135–1144. ⟨https://doi.org/10.1180/minmag.2016.080.085⟩.
[46] A. Pfitzner, Cu_3SbSe_3: synthese und kristallstruktur, Z. Anorg. Allg. Chem. 621 (1995) 685–688, https://doi.org/10.1002/zaac.19956210431
[47] P.W. Majsztrik, M. Kirkham, V. Garcia-Negron, E. Lara-Curzio, E.J. Skoug, D.T. Morelli, Effect of thermal processing on the microstructure and composition of Cu-Sb-Se compounds, J. Mater. Sci. 48 (2013) 2188–2198, https://doi.org/10.1007/s10853-012-6994-x
[48] O. Redlich, A.T. Kister, Algebraic representation of thermodynamic properties and the classification of solutions, Ind. Eng. Chem. 40 (1948) 345–348, https://doi.org/10.1021/ie50458a036
[49] V.I. Lutsyk, V.P. Vorob'eva, 3D model of the T-x-y diagram of the Bi-In-Sn system for designing microstructure of alloys, Russ. J. Inorg. Chem. 61 (2016) 188–207, https://doi.org/10.1134/S0036023616020121
[50] V.I. Lutsyk, V.P. Vorob'eva, Computer models of eutectic-type T-x-y diagrams with allotropy, J. Therm. Anal. Calorim. 101 (2010) 25–31, https://doi.org/10.1007/s10973-010-0855-0
[51] E.Y. Moshchenskaya, V.V. Slepushkin, Method for constructing liquidus curves of binary eutectic systems, Russ. J. Inorg. Chem. 60 (2015) 74–79, https://doi.org/10.1134/S0036023615010088
[52] Y. Li, W. Zhu, Q. Li, S. Qiu, J. Zhang, Phase equilibria in the Nb-Ti side of the Nb-Si-Ti system at 1200°C and its oxidation behavior, J. Alloy. Compd. 704 (2017) 311–321, https://doi.org/10.1016/j.jallcom.2017.02.007
[53] C.A. Utton, I. Papadimitriou, H. Kinoshita, P. Tsakiropoulos, Experimental and thermodynamic assessment of the Ge-Nb-Si ternary phase diagram, J. Alloy. Compd. 717 (2017) 303–316, https://doi.org/10.1016/j.jallcom.2017.04.279
[54] M. Premovic, Y. Du, D. Minic, C. Zhang, D. Manasijevic, L. Balanovic, I. Markovic, Experimental investigation and thermodynamic calculation of the Cu-Ge-Sb system, J. Alloy. Compd. 726 (2017) 820–832, https://doi.org/10.1016/j.jallcom.2017.08.051
[55] G. Cacciamani, G. Roncallo, Y. Wang, E. Vacchieri, A. Costa, Thermodynamic modelling of a six component (C-Co-Cr-Ni-Ta-W) system for the simulation of Cobalt based alloys, J. Alloy. Compd. 730 (2018) 291–310, https://doi.org/10.1016/j.jallcom.2017.09.327
[56] O.V. Andreev, V.B. Kharitontsev, A.A. Polkovnikov, A.V. Elyshev, P.O. Andreev, Phase diagram of the Y-Y_2Se_3 system, enthalpies of phase transformations, J. Solid State Chem. 230 (2015) 186–190, https://doi.org/10.1016/j.jssc.2015.06.042
[57] O.V. Andreev, V.V. Atuchin, A.S. Aleksandrovsky, Y.G. Denisenko, B.A. Zakharov, A.P. Tyutyunnik, N.N. Habibullayev, D.A. Velikanov, D.A. Ulybin, D.D. Shpindyuk, Synthesis, structure, and properties of $EuLnCuSe_3$ (Ln = Nd, Sm, Gd, Er), Crystals 12 (2022) 17, https://doi.org/10.3390/cryst12010017
[58] O.V. Andreev, V.B. Kharitontsev, A.V. Elyshev, Compositions of phases in the interaction of rare-earth metals with selenium, Russ. J. Inorg. Chem. 58 (2013) 910–914, https://doi.org/10.1134/S0036023613080020
[59] A.S. Panfilov, G.E. Grechnev, D.A. Chareev, A.A. Polkovnikov, O.V. Andreev, Pressure effect on magnetic susceptibility of SmS in the "black" phase, J. Alloy. Compd. 695 (2017) 1647–1652, https://doi.org/10.1016/j.jallcom.2016.10.311
[60] P.O. Andreev, L.A. Pimneva, Y_2S_3-Y_2O_3 phase diagram and the enthalpies of phase transitions, J. Solid State Chem. 263 (2018) 24–29, https://doi.org/10.1016/j.jssc.2018.03.001

[61] S. Chen, W. Cao, F. Zhang, Q. Li, J. Zhang, C. Zhang, J. Zhu, Calculation of 2D and 3D phase diagrams, JOM 67 (2015) 1876–1880, https://doi.org/10.1007/s11837-015-1490-9
[62] Q. Luo, C. Zhai, D. Sun, W. Chen, Q. Li, Interpolation and extrapolation with the CALPHAD method, J. Mater. Sci. 35 (2019) 2115–2120, https://doi.org/10.1016/j.jmst.2019.05.016
[63] S. Chen, W. Cao, C. Zhang, J. Zhu, F. Zhang, Q. Li, J. Zhang, Calculation of property contour diagrams, CALPHAD Comput. Coupling Phase Diagr. Thermochem. 55 (2016) 63–68, https://doi.org/10.1016/j.calphad.2016.05.004
[64] Y.G. Lavrent'ev, N.S. Karmanov, L.V. Usova, Electron probe microanalysis of minerals: microanalyzer or scanning electron microscope? Russ. Geol. Geophys. 56 (2015) 1154–1161, https://doi.org/10.1016/j.rgg.2015.07.006
[65] M. Wang, C. Wang, Bulk properties of biomaterials and testing techniques, in: Roger Narayan (Ed.), Encyclopedia of Biomedical Engineering, Elsevier, 2019, pp. 53–64, https://doi.org/10.1016/B978-0-12-801238-3.99861-1
[66] P.O. Andreev, A.A. Polkovnikov, Y.G. Denisenko, O.V. Andreev, T.M. Burkhanova, A.N. Bobylev, L.A. Pimneva, Temperatures and enthalpies of melting of Ln_2S_3 (Ln=Gd, Tb, Dy, Ho, Er, Tm, Yb, and Lu) compounds, J. Therm. Anal. Calorim. 131 (2018) 1545–1551, https://doi.org/10.1007/s10973-017-6620-x
[67] I.A. Razumkova, O.V. Andreev, Sc_2S_3-Cu_2S phase diagram, Russ. J. Inorg. Chem. 61 (2016) 1035–1040, https://doi.org/10.1134/S0036023616080131
[68] I.A. Razumkova, A.N. Boiko, O.V. Andreev, S.A. Basova, Synthesis of $[(H_3O)Tm_3F_{10}]\cdot nH_2O$, ErF_3, and TmF_3 powders and their physicochemical properties, Russ. J. Inorg. Chem. 62 (2017) 418–422, https://doi.org/10.1134/S0036023617040155
[69] J.C.P. Santos, N. Chaia, K.E. Borowski, A.A.A.P. Silva, D.F. Barros, D.A. Abreu, C.A. Nunes, G.C. Coelho, Experimental investigation of phase equilibria at 1200°C in the Al-Nb-V system, J. Phase Equilib. Diffus. 41 (2020) 172–180, https://doi.org/10.1007/s11669-020-00802-8
[70] J.P.M. van der Meer, R.J.M. Konings, M.H.G. Jacobs, H.A.J. Oonk, A miscibility gap in LiF-BeF_2 and LiF-BeF_2-ThF_4, J. Nucl. Mater. 344 (2005) 94–99, https://doi.org/10.1016/j.jnucmat.2005.04.023
[71] L.L. Kotomin, P.Y. Orlov, S.S. Sikerin, E.A. Olennikov, The computer graph of the phase diagrams, in: Materials Science International Services GmbH, Stuttgart (2004) (Eds.), Phase Diagrams in Materials Science: Proceedings of the 6th International School-Conference in Material Science PDMS VI-2001 (October 14–20, 2001, Kiev, Ukraine), p. 214.
[72] D. Jendrzejczyk-Handzlik, P. Handzlik, K. Fitzner, Experimental investigations of phase equilibria in ternary Ag-Cu-Ga system, J. Phase Equilib. Diffus. 40 (2019) 64–78, https://doi.org/10.1007/s11669-018-0697-1
[73] K. Knorr, N. Yang, Quantitative X-ray mineralogy of iron ore and scales, in: K. McShane, A. Salerno, O.T. Fong (Eds.), Proceedings of the Iron Ore Conference 2011 (11–13 July, Perth, Western Australia), The Australasian Institute of Mining and Metallurgy (The AusIMM), 2011, pp. 265–269. ⟨https://www.researchgate.net/publication/229812188⟩.
[74] D.A. Aksenov, R.N. Asfandiyarov, G.I. Raab, E.I. Fakhretdinova, M.A. Shishkunova, Influence of the chromium content in low-alloyed Cu-Cr alloys on the structural changes, phase transformations and properties in equal-channel angular pressing, Metals 11 (2021) 1795, https://doi.org/10.3390/met11111795
[75] M.R. Rowles, The effect of data quality and model parameters on the quantitative phase analysis of X-ray diffraction data by the Rietveld method, J. Appl. Crystallogr. 54 (2021) 878–894, https://doi.org/10.1107/S160057672100371X
[76] T. Degen, M. Sadki, E. Bron, U. König, G. Nénert, The HighScore suite, Powder Diffr. 29 (S2) (2014) S13–S18, https://doi.org/10.1017/S0885715614000840
[77] J. Rodrıguez-Carvajal, Recent Developments of the Program Fullprof, IUCr Commission on Powder Diffraction Newsletter, 2001, pp. 12–19 ⟨https://scholar.google.com/scholar?hl=en&as_sdt=0,5&cluster=2865552527093501896⟩.
[78] Paolo Scardi, Diffraction line profiles in the Rietveld method, Cryst. Growth Des., 20, 2020, pp. 6903–6916. ⟨https://dx.doi.org/10.1021/acs.cgd.0c00956⟩.
[79] A.A. Coelho, TOPAS and TOPAS-academic: an optimization program integrating computer algebra and crystallographic objects written in C++, J. Appl. Crystallogr. 51 (1) (2018) 210–218, https://doi.org/10.1107/S1600576718000183
[80] P. Scardi, C.L. Azanza Ricardo, C. Perez-Demydenko, A.A. Coelho, Whole powder pattern modelling macros for TOPAS, J. Appl. Crystallogr. 51 (2018) 1752–1765, https://doi.org/10.1107/S160057671801289X
[81] R.S. Bubnova, V.A. Firsova, S.K. Filatov, Software for determining the thermal expansion tensor and the graphic representation of its characteristic surface (Theta to Tensor-TTT), Glass Phys. Chem. 39 (2013) 347–350, https://doi.org/10.1134/S108765961303005X
[82] R.S. Bubnova, V.A. Firsova, S.N. Volkov, S.K. Filatov, RietveldToTensor: program for processing powder X-ray diffraction data under variable conditions, Glass Phys. Chem. 44 (2018) 33–40, https://doi.org/10.1134/S1087659618010054
[83] Gemini R Ultra User Manual, Version 1.6, Oxford Diffraction, Oxford, UK, 2006.
[84] Rigaku OD, CrysAlisPro. Yarnton, England: Rigaku-Oxford Diffraction Ltd, 2019. ⟨https://www.rigaku.com/products/crystallography/crysalis⟩. (Accessed 29 September 2021).
[85] G.M. Sheldrick, SHELXT – integrated space-group and crystal-structure determination, Acta Crystallogr. A 71 (2015) 3–8, https://doi.org/10.1107/S2053273314026370
[86] G.M. Sheldrick, Crystal structure refinement with SHELXL, Acta Crystallogr. C 71 (2015) 3–8, https://doi.org/10.1107/S2053229614024218
[87] C.B. Hübschle, G.M. Sheldrick, B. Dittrich, ShelXle: a Qt graphical user interface for SHELXL, J. Appl. Crystallogr. 44 (2011) 1281–1284, https://doi.org/10.1107/S0021889811043202
[88] A.L. Spek, checkCIF validation ALERTS: what they mean and how to respond, Acta Crystallogr. E 76 (2020) 1–11, https://doi.org/10.1107/S2056989019016244
[89] K. Momma, F. Izumi, VESTA 3 for three-dimensional visualization of crystal, volumetric and morphology data, J. Appl. Crystallogr. 44 (2011) 1272–1276, https://doi.org/10.1107/S0021889811038970
[90] C.R. Groom, I.J. Bruno, M.P. Lightfoot, S.C. Ward, The Cambridge structural database, Acta Crystallogr. B 72 (2016) 171–179, https://doi.org/10.1107/S2052520616003954
[91] L.C. Sim, J.M. Khor, K.H. Leong, P. Saravanan, Synthesis and characterization of dried leaves derived carbon quantum dots and g-C3N4 composite, IOP Conf. Ser. Mater. Sci. Eng. 894 (2020) 012003, https://doi.org/10.1088/1757-899X/894/1/012003
[92] S. Rampino, F. Pattini, M. Bronzoni, M. Mazzer, M. Sidoli, G. Spaggiari, E. Gilioli, $CuSbSe_2$ thin film solar cells with ~4% conversion efficiency grown by low-temperature pulsed electron deposition, Sol. Energy Mater. Sol. Cells 185 (2018) 86–96, https://doi.org/10.1016/j.solmat.2018.05.024
[93] P. Škácha, J. Sejkora, J. Plášil, Příbramite, CuSbSe2, the Se-analogue of chalcostibite, a new mineral from Příbram, Czech Republic, Eur. J. Mineral. 29 (2017) 653–661, https://doi.org/10.1127/ejm/2017/0029-2623
[94] E. Chavarriaga, N. Correa, J. Montoya, O. Restrepo, Color prediction in ceramic enamels using the Kubelka Munk Model, Tecciencia 10 (2015) 1–5, https://doi.org/10.18180/tecciencia.2015.19.1
[95] T.-R. Wei, C.-F. Wu, W. Sun, Y. Pana, J.-F. Li, Is Cu_3SbSe_3 a promising thermoelectric material? RSC Adv. 5 (2015) 42848–42854, https://doi.org/10.1039/C5RA03953C
[96] O.V. Lapshin, E.V. Boldyreva, V.V. Boldyrev, Role of mixing and milling in mechanochemical synthesis, Russ. J. Inorg. Chem. 66 (2021) 433–453, https://doi.org/10.1134/S0036023621030116
[97] A.A. Michalchuk, E.V. Boldyreva, A.M. Belenguer, F. Emmerling, V.V. Boldyrev, Tribochemistry, mechanical alloying, mechanochemistry: what is in a name? Front. Chem. 9 (2021) 685789, https://doi.org/10.3389/fchem.2021.685789
[98] Y. Guo, B. Liu, W. Xie, Q. Luo, Q. Li, Anti-phase boundary energy of β series precipitates in Mg-Y-Nd system, Scr. Mater. 193 (2021) 127–131, https://doi.org/10.1016/j.scriptamat.2020.11.004
[99] Y. Pang, D. Sun, Q. Gu, K.-C. Chou, X. Wang, Q. Li, Comprehensive determination of kinetic parameters in solid-state phase transitions: an extended Jonhson-Mehl-Avrami-Kolomogorov model with analytical solutions, Cryst. Growth Des. 16 (2016) 2404–2415, https://doi.org/10.1021/acs.cgd.6b00187
[100] Q. Luo, Y. Guo, B. Liu, Y. Feng, J. Zhang, Q. Li, K. Chou, Thermodynamics and kinetics of phase transformation in rare earth-magnesium alloys: a critical review, J. Mater. Sci. 44 (2020) 171–190, https://doi.org/10.1016/j.jmst.2020.01.022
[101] T. Xie, H. Shi, H. Wang, Q. Luo, Q. Li, K.-C. Chou, Thermodynamic prediction of thermal diffusivity and thermal conductivity in Mg-Zn-La/Ce system, J. Mater. Sci. 97 (2022) 147–155, https://doi.org/10.1016/j.jmst.2021.04.044
[102] P.J. Haines, M. Reading, F.W. Wilburn, Chapter 5 – differential thermal analysis and differential scanning calorimetry, in: M.E. Brown (Ed.), Handbook of Thermal Analysis and Calorimetry, Vol. 1 Elsevier Science B.V., Amsterdam, The Netherlands, 1998, pp. 279–361, https://doi.org/10.1016/S1573-4374(98)80008-3
[103] A.W. Sleight, Thermal contraction, Endeavour 19 (1995) 64–68, https://doi.org/10.1016/0160-9327(95)93586-4
[104] A.W. Sleight, Compounds that contract on heating, Inorg. Chem. 37 (1998) 2854–2860, https://doi.org/10.1021/ic980253h
[105] S.K. Filatov, R.S. Bubnova, The nature of special points on unit cell parameters temperature dependences for crystal substances, in: Deutsche Gesellschaft für Kristallographie (Eds.), Proceedings of the Tenth European Powder Diffraction Conference, Geneva, 1–4 September 2006, Oldenbourg Wissenschaftsverlag, München, 2015, pp. 447–452. ⟨https://doi.org/10.1524/9783486992540-070⟩.
[106] S.K. Filatov, Negative linear thermal expansion of oblique-angle (monoclinic and triclinic) crystals as a common case, Phys. Status Solidi (b) 245 (2008) 2490–2496, https://doi.org/10.1002/pssb.200880256
[107] S.K. Filatov, S.V. Krivovichev, R.S. Bubnova, Sistematicheskaya Kristallokhimiya (Systematics Crystal Chemistry), SPBU Publishing, Saint-Petersburg, 2019, p. 231. ⟨https://pureportal.spbu.ru/en/publications/систематическая-кристаллохимия⟩. (Accessed 23 January 2022).
[108] D.N. Kamaev, Modelirovanie diagrammy sostoyaniya sistemy BeO-Al_2O_3 (modelling of the phase equilibriums in the system BeO-Al_2O_3), Rasplavyi (2019) 265–271, https://doi.org/10.1134/S0235010619030071
[109] G.G. Mikhailov, B.I. Leonovich, Y.S. Kuznetsov, Termodynamica metallurgicheskih processov i system (Thermodynamics of Metallurgical Processes and Systems), MISA Publications, Moscow, 2009, p. 520. ⟨https://scholar.google.com/scholar?hl=ru&as_sdt=0%2C5&q=G.G.+Mikhailov%2C+B.I.+Leonovich%2C+Y.S.+Kuznetsov%2C+Thermodynamics+of+metallurgical+processes+and+systems&btnG=⟩. (Accessed 20 January 2022).
[110] D.N. Kamaev, Termodinamicheskoe modelirovanie diagrammyi sostoyaniya sistemyi NaCl-$BeCl_2$ (thermo dynamical modeling of binary constitution diagram of NaCl-$BeCl_2$ system), Rasplavyi (2010) 44–48 ⟨https://www.elibrary.ru/item.asp?id=13423290⟩ (Accessed 20 January 2022).
[111] N.O. Azarapin, A.S. Aleksandrovsky, V.V. Atuchin, T.A. Gavrilova, A.S. Krylov, M.S. Molokeev, S. Mukherjee, A.S. Oreshonkov, O.V. Andreev, Synthesis, structural and spectroscopic properties of orthorhombic compounds $BaLnCuS_3$ (Ln=Pr, Sm), J. Alloy. Compd. 832 (2020) 153134, https://doi.org/10.1016/j.jallcom.2019.153134